



HAL
open science

Fast high-fidelity single-shot readout of spins in silicon using a single-electron box

G.A. Oakes, V.N. Ciriano-Tejel, D. Wise, M.A. Fogarty, T. Lundberg, C. Lainé, S. Schaal, F. Martins, D.J. Ibberson, L. Hutin, et al.

► **To cite this version:**

G.A. Oakes, V.N. Ciriano-Tejel, D. Wise, M.A. Fogarty, T. Lundberg, et al.. Fast high-fidelity single-shot readout of spins in silicon using a single-electron box. *Physical Review X*, 2023, 13 (1), pp.011023. 10.1103/PhysRevX.13.011023 . hal-03623278

HAL Id: hal-03623278

<https://hal.science/hal-03623278v1>

Submitted on 20 Sep 2024

HAL is a multi-disciplinary open access archive for the deposit and dissemination of scientific research documents, whether they are published or not. The documents may come from teaching and research institutions in France or abroad, or from public or private research centers.

L'archive ouverte pluridisciplinaire **HAL**, est destinée au dépôt et à la diffusion de documents scientifiques de niveau recherche, publiés ou non, émanant des établissements d'enseignement et de recherche français ou étrangers, des laboratoires publics ou privés.



Distributed under a Creative Commons Attribution 4.0 International License

Fast High-Fidelity Single-Shot Readout of Spins in Silicon Using a Single-Electron Box

G. A. Oakes^{1,2,*} V. N. Ciriano-Tejel,^{2,3,*} D. F. Wise,^{2,3} M. A. Fogarty,^{2,3} T. Lundberg,^{1,4} C. Lainé,^{2,3} S. Schaal,^{2,3} F. Martins⁴ D. J. Ibberson,^{5,4} L. Hutin,⁶ B. Bertrand⁶ N. Stelmashenko,⁷ J. W. A. Robinson,⁷ L. Ibberson⁴ A. Hashim,⁸ I. Siddiqi,⁸ A. Lee,¹ M. Vinet,⁶ C. G. Smith^{1,4} J. J. L. Morton,^{2,3,†} and M. F. Gonzalez-Zalba^{2,‡}

¹*Cavendish Laboratory, University of Cambridge,*

J.J. Thomson Avenue, Cambridge CB3 0HE, United Kingdom

²*Quantum Motion, 9 Sterling Way, London N7 9HJ, United Kingdom*

³*London Centre for Nanotechnology, University College London, London WC1H 0AH, United Kingdom*

⁴*Hitachi Cambridge Laboratory, J.J. Thomson Avenue, Cambridge CB3 0HE, United Kingdom*

⁵*Quantum Engineering Technology Labs, University of Bristol,*


Tyndall Avenue, Bristol BS8 1FD, United Kingdom

⁶*CEA, LETI, Minatec Campus, F-38054 Grenoble, France*

⁷*Department of Materials Science and Metallurgy, University of Cambridge,*

27 Charles Babbage Road, Cambridge CB3 0FS, United Kingdom

⁸*Quantum Nanoelectronics Laboratory, Department of Physics, University of California, Berkeley, California 94720, USA*

 (Received 7 May 2022; revised 4 December 2022; accepted 5 January 2023; published 23 February 2023)

Three key metrics for readout systems in quantum processors are measurement speed, fidelity, and footprint. Fast high-fidelity readout enables midcircuit measurements, a necessary feature for many dynamic algorithms and quantum error correction, while a small footprint facilitates the design of scalable, highly connected architectures with the associated increase in computing performance. Here, we present two complementary demonstrations of fast high-fidelity single-shot readout of spins in silicon quantum dots using a compact, dispersive charge sensor: a radio-frequency single-electron box. The sensor, despite requiring fewer electrodes than conventional detectors, performs at the state of the art achieving spin readout fidelity of 99.2% in less than 6 μs fitted from a physical model. We demonstrate that low-loss high-impedance resonators, highly coupled to the sensing dot, in conjunction with Josephson parametric amplification are instrumental in achieving optimal performance. We quantify the benefit of Pauli spin blockade over spin-dependent tunneling to a reservoir, as the spin-to-charge conversion mechanism in these readout schemes. Our results place dispersive charge sensing at the forefront of readout methodologies for scalable semiconductor spin-based quantum processors.

DOI: 10.1103/PhysRevX.13.011023

Subject Areas: Condensed Matter Physics, Electronics, Semiconductor Physics

I. INTRODUCTION

Electron spin qubits in silicon are consolidating their position as a leading candidate to build scalable high-fidelity quantum processors. Several recent demonstrations have shown single- and two-qubit gate fidelities exceeding the requirements for fault-tolerant thresholds in the same device [1–3]. Combined with the dense

scaling potential [4,5], advanced manufacturing [6,7], and prospects for integration with cryogenic classical electronics [8], these results present a promising future for spin-based qubits in silicon.

For universal quantum computing, the technology will require fast high-fidelity readout on a timescale which is short compared to the qubit coherence time to allow for error correction codes to be implemented. Even for noisy intermediate-scale quantum processors, fast measurement remains advantageous to avoid readout becoming the bottleneck in circuit run-time and to enable midcircuit measurements for error mitigation [9,10] and gate teleportation [11].

Fast spin readout has been shown using single-electron transistors (SETs) with spin-readout fidelities as high as 99.9% in 6 μs [12] and 99% in 1.6 μs in radio-frequency (rf) mode [13]. However, a SET requires at least three

*These authors contributed equally to this work.

†john@quantummotion.tech

‡fernando@quantummotion.tech

Published by the American Physical Society under the terms of the [Creative Commons Attribution 4.0 International license](https://creativecommons.org/licenses/by/4.0/). Further distribution of this work must maintain attribution to the author(s) and the published article's title, journal citation, and DOI.

electrodes and two charge reservoirs significantly limiting their placement within dense qubit arrays.

Dispersive readout methods, based on detecting alternating single-electron currents, offer the benefit that only two electrodes are needed to either sense the system *in situ* using Pauli spin blockade (PSB) [14–16] or to create a dispersive charge sensor, i.e., a single-electron box (SEB), to read the target qubit [17–21]. These methods require zero or one charge reservoirs, respectively, strongly enhancing their capacity to be introduced within qubit arrays. The SEB, however, offers the key technological advantage it can detect electronic transitions occurring at rates much lower than the probing rf frequency, which could be the case in the few-electron regime where qubits are operated. However, the performance of SEBs in silicon (99.2% in 100 μs [22]) has remained noncompetitive with respect to SETs, raising the question of whether fast and compact high-fidelity readout could be possible.

Here, we present two independent demonstrations showing that the compact SEB electrometer can achieve fast and accurate spin readout in silicon, reaching 99.2% fidelity in just 5.6 μs , obtained from a fit to standard physical models. This result compares favorably to the state-of-the-art dispersive readout of 97% in 6 μs [23]. Our work spans four key aspects in designing optimal dispersive charge sensors: (i) the SEB design, (ii) the readout resonator design, (iii) the physical mechanism for spin-to-charge conversion, and (iv) the amplification chain. We present SEBs with large gate couplings (i) coupled to low-loss high-impedance rf resonators (ii). We show the benefits of Pauli spin blockade readout over spin-dependent tunneling to a reservoir (iii) and demonstrate the role of parametric amplification in improving dispersive readout fidelity (iv). These results demonstrate a route to combining high-fidelity readout of semiconductor-based qubits with the demands of a compact and scalable architecture.

II. OPTIMIZING READOUT SENSITIVITY

Dispersive charge sensing using a SEB works on the principle of some change ΔC_D in the quantum capacitance of the SEB arising from a change in its local electrostatic environment. This capacitance shift is detected via a change in the reflected power ΔP_{rf} of a rf signal from a resonator whose frequency depends on C_D . The sensitivity of the SEB can be characterized by the ratio of the signal and noise powers, $\text{SNR} = \Delta P_{\text{rf}}/P_n$, where P_n is the noise power. In order to maximize the SNR, the available strategies are to minimize the noise power or to maximize the signal power. As we shall see later, the signal power is enhanced by (i) increasing the gate lever arm of the SEB α (defined as the ratio of the gate capacitance of the SEB and its total capacitance) and its capacitive coupling to the spin system to be sensed, and by (ii) optimizing the resonator design which involves a well-matched, low-loss, high-

impedance resonator, operating at high frequency but kept below the tunneling rate of the SEB. More details on the dependence of the SNR on each of these parameters are given below [see Eq. (3) and Appendix A]. Further, for a theoretical SNR comparison between the SEB and dispersive readout, and the SEB and the SET, see Appendixes A and B, respectively.

Here, we present different approaches to increasing the SNR by optimization of these parameters and compare two strategies for converting the spin degree of freedom of the qubit into a charge event which can be detected by the SEB. We begin by using spin-dependent tunneling while minimizing the noise power P_n through the use of a Josephson parametric amplifier (JPA) [24].

III. SPIN-DEPENDENT TUNNELING

The device in this section is an etched silicon nanowire double split-gate transistor that, at low temperatures, can be used to form quantum dots (QDs) at the upper edges of the nanowire, one under each of the four gates [see Fig. 1(a) and Appendix C for device dimensions]. One of the gates is connected to a lumped-element resonator to form a SEB that is used as a charge sensor to measure the qubit—here, the spin of an electron confined under the gate opposite to the SEB—using spin-dependent tunneling. The other two gates are not used. Changes in the SEB quantum capacitance C_D are detected via rf reflectometry [25], where a tone of frequency f_{rf} is delivered through an attenuated line to the lumped resonator [see Fig. 1(a)] capacitively coupled to the transmission line ($C_c = 50$ fF). The resonator, of natural frequency $f_{\text{res}} = 665.5$ MHz at 2 T, consists of a spiral NbN inductor ($L = 124 \pm 4$ nH) and the parasitic capacitance ($C_p = 410$ fF) in parallel with the SEB and presents an internal Q factor, $Q_0 = 270$, a high-impedance $Z_r = 520$ Ω , and a coupling coefficient $\beta = 2.5$ (see Appendix D for the setup and Appendix E for more information about the resonator).

The SEB, with an $\alpha = 0.35$, is strongly sensitive to the “qubit dot” [as shown in Fig. 1(b)], meaning that the addition of one electron to the QD causes a change in the quantum capacitance of the SEB which shifts its response by more than one linewidth. This shift is used to perform spin readout using the three-level pulse sequence illustrated in Figs. 1(b) and 1(c).

The noise of the system (conveniently characterized by the equivalent noise temperature T_n) contains contributions from the system itself T_{sys} (SEB and resonator) as well as the amplification chain [see Fig. 1(a)]. In rf measurements of semiconductor QDs, a high-mobility electron transistor (HEMT) is typically used as the first amplifier, limiting the noise temperature to a few kelvin. Here we add an amplifier with lower noise temperature, a JPA, with gain G_{JPA} , reducing T_n accordingly:

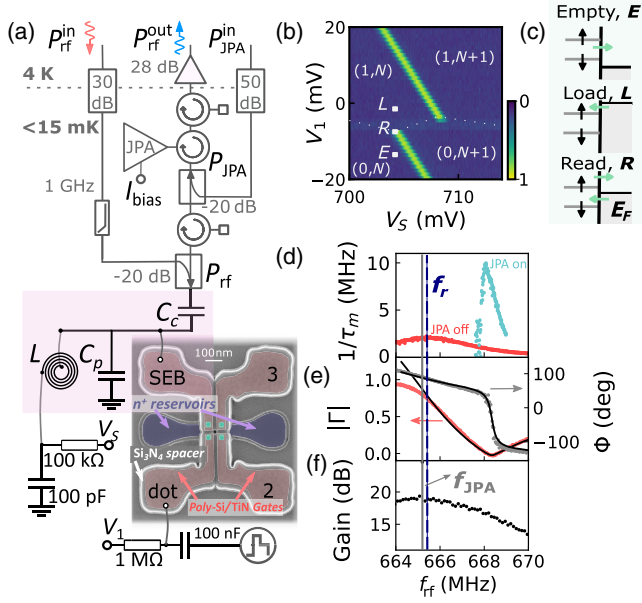


FIG. 1. Device and measurement setup. (a) False-color scanning electron micrograph of a silicon nanowire transistor with two pairs of split gates (red). The green dots indicate the location of the QDs under each gate. The blue regions are electron reservoirs. The SEB is connected to a lumped-element resonator and the fast pulses for spin-dependent readout are applied to the dot facing it through a bias tee. See Appendix D for more information about the measurement setup. (b) Normalized rf response of the stability diagram of the SEB and the dot. The SEB potential shifts when the first electron is added to the dot, changing the rf response from a maximum to some minimum, background level. (c) The dot is first emptied (E) so an electron with a random spin polarization enters the dot at the load stage (L). Finally, the spin polarization is measured (R) by placing the reservoir in between the $|\uparrow\rangle$ and $|\downarrow\rangle$ states. (d) The inverse of the minimum integration time $1/\tau_m$ for a $\text{SNR} = 1$ is shown as a function of f_{rf} without and with the JPA (red and blue, respectively). The black dashed line indicates the natural frequency of the resonator f_{res} , which optimizes sensitivity without the JPA. (e) The reflection coefficient [magnitude $|\Gamma|$ (red) and phase Φ (gray)] at $B = 2$ T shows a minimum at the frequency which optimizes sensitivity with the JPA. (f) The JPA gain decreases as f_{rf} moves away from the JPA pumping frequency f_{JPA} , solid gray line, as determined by the JPA bandwidth of 19.2 MHz.

$$T_n = T_{\text{sys}} + T_{\text{JPA}} + \frac{T_{\text{HEMT}}}{G_{\text{JPA}}}, \quad (1)$$

where $T_{\text{HEMT(JPA)}}$ is the noise temperature of the HEMT (JPA). We note the use of a JPA is only advantageous if the noise is dominated by the HEMT instead of the system. This is not the case for rf SETs where shot noise may be comparable or in excess of that of the HEMT [26]. For SEBs, if the tunneling rate γ between SEB and reservoir is greater than f_{rf} , electrons tunnel adiabatically, and the Sisyphus noise is substantially reduced [16] leaving

predominantly the noise contribution of the HEMT (see Appendix F for a description of the JPA).

In this device, the tunneling rate γ between SEB and reservoir is 74 ± 12 GHz (see Appendix G), well in excess of $f_{\text{rf}} \sim 0.7$ GHz, such that we are in the regime of negligible Sisyphus dissipation in the SEB. This is confirmed by noise temperature measurements yielding $T_n = 2.5^{+1.4}_{-0.9}$ K [27] with the JPA off, reducing to $T_n = 0.25^{+0.14}_{-0.09}$ K with the JPA. The fact that the latter falls below typical shot noise levels [26] demonstrates one of the major advantages of SEBs over SETs. This tenfold reduction of noise temperature with the JPA leads to a corresponding reduction in τ_m , the minimum integration time to resolve a charge event with a $\text{SNR} = 1$ [28]. When measuring at $f_{\text{rf}} = 668$ MHz, where the reflection coefficient of the resonant circuit is at a minimum, we find $\tau_m = 1$ μs and $\tau_m = 100$ ns, for JPA off and on, respectively. Operating at this point of minimum reflected power is necessary to avoid driving the JPA beyond its 1 dB compression point, $P_{1 \text{ dB}} = -116$ dBm. However, as can be seen in Fig. 1(d), τ_m with the JPA off can be decreased by approximately a factor of 2 by adjusting the drive frequency f_{rf} to match f_{res} , which differs from the point of minimum reflected power in the total circuit. The overall achievable reduction in τ_m achieved using the JPA is therefore a factor of 4.5 (see Appendix H for more details). These results emphasize the importance of a well-matched and high- Q resonator to minimize the reflected power to avoid saturating the JPA [27]. The limit in measurement bandwidth is set by the difference Δf between the JPA pump frequency ($f_{\text{JPA}} = 665.2$ MHz) and f_{rf} , while the JPA gain falls as this difference increases [see Fig. 1(f)]. We select $\Delta f = 2.9$ MHz for which $G_{\text{JPA}} = 17$ dB.

A. Spin readout and fidelity

To measure the spin of the electron in the QD, we apply a magnetic field of $B = 2$ T to produce a Zeeman splitting $E_Z = g\mu_B B$ larger than the thermal broadening of the reservoir into which the electrons tunnel. Here, $T_e = 137 \pm 18$ mK is the electron temperature (see Appendix I), μ_B is the Bohr magneton, and $g \approx 2$ is the electron g factor. To measure the spin orientation, we apply a three-level voltage pulse to the QD gate [see inset of Fig. 1(b) and 1(c)]. First, the QD is emptied so an electron with a random spin polarization can be loaded from the reservoir. Then, at the readout stage, the reservoir Fermi energy E_F lies in between the spin $|\uparrow\rangle$ and $|\downarrow\rangle$ states, so a spin $|\uparrow\rangle$ electron can tunnel out from the dot to the reservoir and be subsequently replaced by a spin $|\downarrow\rangle$ electron, whereas a spin $|\downarrow\rangle$ electron remains in the QD [29]. During the readout stage, the system is tuned at the position marked R in Fig. 1(b), where the SEB rf response is strongly dependent on the QD electronic occupation. This way, a readout trace from a spin $|\downarrow\rangle$ state is a constant noisy background [the gray and black traces in Fig. 2(a)]. On the

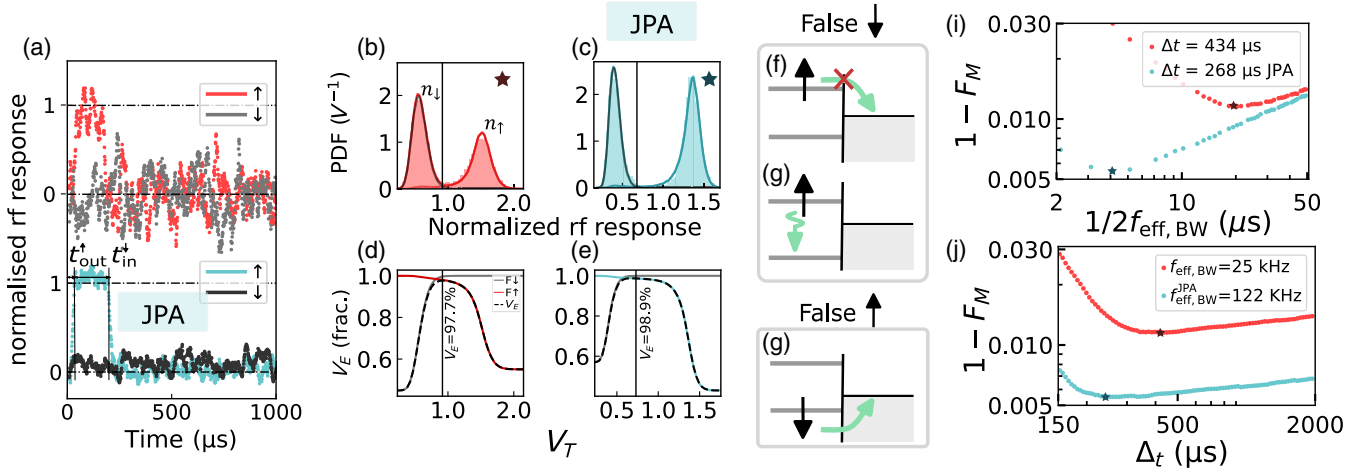


FIG. 2. Spin readout fidelity. (a) Top: spin $|\uparrow\rangle$ (red) and $|\downarrow\rangle$ (gray) traces taken without the JPA. The rf response is normalized so it is 0 when the dot is occupied and 1 when it is empty. The bottom panel shows spin $|\uparrow\rangle$ (blue) and spin $|\downarrow\rangle$ (black) traces taken with a JPA. (b) Histogram of the maximum values of the normalized rf response from 10 000 single-shot measured data traces taken without a JPA. The red line is the simulated histogram created using the parameters $A = 0.50$, $\Gamma_s = 1$ MHz, $t_{\text{out}}^\uparrow = 53$ μs , $t_{\text{in}}^\uparrow = 440$ μs , and Gaussian noise with standard deviation $\sigma_{\text{high}} = 1.09$ for the top of the blip and $\sigma_{\text{low}} = 1.03$ for the background. Both the measurement bandwidth and readout time used to create this histogram correspond with the optimal $\Delta t = 434$ μs and measurement bandwidth $f_{\text{eff,BW}} = 25$ kHz. (c) Same as (b) for measurement taken with a JPA. In this case, the parameters used for the simulation are $A_{\text{JPA}} = 0.46$, $\Gamma_{s,\text{JPA}} = 1$ MHz, $t_{\text{out,JPA}}^\uparrow = 31$ μs , $t_{\text{in,JPA}}^\downarrow = 186$ μs , and Gaussian noise with standard deviation $\sigma_{\text{high,JPA}} = 0.38$ for the top of the blip and $\sigma_{\text{low,JPA}} = 0.36$ for the background. The postprocessing parameters are chosen to be the ones that maximize the visibility ($\Delta t = 268$ μs and $f_{\text{eff,BW}}^{\text{JPA}} = 122$ kHz). (d) Electrical visibility V_E as a function of the threshold voltage used to discriminate between spin down and up. (e) Same for traces obtained using a JPA. (f)–(h) Spin mapping errors due to long readout time with respect to $t_{\text{out}}^\downarrow$ (f), relaxation processes (g), or thermal excitations (h). (i) Measurement infidelity ($1 - F_M$) taken with (blue) and without (red) a JPA as a function of the integration time, which is equal to $1/2f_{\text{eff,BW}}$. (j) Measurement infidelity versus measurement time Δt . The stars mark the optimal integration times and measurement times.

other hand, a spin $|\uparrow\rangle$ readout trace is characterized by a top hat shape that starts when the spin $|\uparrow\rangle$ electron leaves the dot (t_{out}^\uparrow), and lasts until a spin $|\downarrow\rangle$ electron tunnels back into the dot (t_{in}^\downarrow). Spin $|\uparrow\rangle$ single-shot traces taken without the JPA are displayed in red in Fig. 2(a), whereas the ones using a JPA in blue show a noticeable $\times 4.5$ SNR improvement. In both cases, the traces are taken with a sample rate of $\Gamma_s = 1$ MHz and a measurement bandwidth of $f_{\text{eff,BW}} = 25$ kHz (see Appendix J for more information about the experiment bandwidth).

We identify the spin polarization of a given trace by setting a threshold in the rf response that is compared against the trace’s maximum. If the threshold is exceeded, the trace is labeled as a spin $|\uparrow\rangle$, and if not, as $|\downarrow\rangle$. The trace’s maxima follow a bimodal probability distribution, as in Figs. 2(b) and 2(c), with one peak corresponding to spin $|\uparrow\rangle$ traces and the other to $|\downarrow\rangle$ traces. To determine the readout fidelity, we model the histograms as $N_{\text{tot}}(V_{\text{rf}}) = N_{\text{tot}}[n_\uparrow(V_{\text{rf}}) + n_\downarrow(V_{\text{rf}})]V_{\text{bin}}$, where $n_{\uparrow(\downarrow)}$ is the probability density of the maxima of spin $|\uparrow\rangle$ ($|\downarrow\rangle$) traces, V_{rf} is the normalized rf response, N_{tot} is the total number of traces, and V_{bin} is the width of the rf response bins [30]. The fidelity of correctly labeling an individual readout trace $F_E^{\uparrow(\downarrow)}$ can be calculated as

$$F_E^\downarrow = 1 - \int_{V_T}^{\infty} n_\downarrow(V_{\text{rf}}) dV_{\text{rf}},$$

$$F_E^\uparrow = 1 - \int_{-\infty}^{V_T} n_\uparrow(V_{\text{rf}}) dV_{\text{rf}}, \quad (2)$$

where the integral of $n_{\downarrow(\uparrow)}$ from $V_T(-\infty)$ to $\infty(V_T)$ is the cumulative probability of having labeled spin $|\downarrow\rangle$ ($|\uparrow\rangle$) trace wrongly [30].

The experimental data result in the bimodal distribution as a whole. However, to obtain n_\uparrow and n_\downarrow separately, we numerically generate 100 000 readout traces, where each trace is assigned a spin polarization with probability A of being spin $|\downarrow\rangle$ and $1 - A$ of being spin $|\uparrow\rangle$. Readout traces are completely determined by a few experimental parameters that can be extracted from the data traces: the sample rate Γ_s , the measurement bandwidth $f_{\text{eff,BW}}$, the sensor SNR, the tunneling times t_{out}^\uparrow and t_{in}^\downarrow , and the readout time Δt (see Appendix K for a description of the parameter extraction). We fit the simulated histogram to 10 000 experimental shots using least squares regression; see Figs. 2(b) and 2(c). In Fig. 2(c), n_\uparrow (solid black curve) and n_\downarrow (solid blue curve) are comparatively narrower due to the reduced noise enabled by the JPA. As shown in Figs. 2(d) and 2(e), the electrical visibility,

$V_E = 1 - F_E^\uparrow - F_E^\downarrow$, depends on the selected threshold voltage V_T . We obtain $V_E = 97.7\%$ without a JPA and $V_E^{\text{JPA}} = 98.9\%$ using a JPA.

Depending on the readout time Δt , spin mapping errors can diminish the readout fidelity. If Δt is of the order or smaller than t_{out}^\uparrow , spin $|\uparrow\rangle$ electrons will not leave the QD during the readout time, leading to a false spin $|\downarrow\rangle$ measurement [see Fig. 2(f)]. On the other hand, if Δt is increased, a spin $|\uparrow\rangle$ may relax to the ground state before leaving the QD, resulting in a false spin $|\downarrow\rangle$ [see Fig. 2(g)], or a spin $|\downarrow\rangle$ could be thermally excited out of the QD, leading to a false spin $|\uparrow\rangle$ [see Fig. 2(h)]. The spin readout fidelity F_M is the product of the electrical fidelity F_E , which determines the probability to label correctly a given readout trace (as discussed earlier), and the spin-to-charge fidelity F_{STC} , setting the probability that a spin state generates the trace that it is expected to. In our case, F_E also includes the false negatives derived from a slow t_{out}^\uparrow , since the simulated traces have a finite length Δt (see Appendix L for a full description).

Having taken spin mapping errors into consideration, we investigate the dependence of F_M on Δt , and $f_{\text{eff,BW}}$ (see Appendix M for a full discussion). Figure 2(i) shows how decreasing $f_{\text{eff,BW}}$ leads to an improved fidelity as the noise is reduced, up to a point in which the additional filtering deforms the spin $|\uparrow\rangle$ top hat, smoothing the edges and reducing its maximum value. The optimal measurement bandwidth is different for measurements taken with and without the JPA not only because of the SNR improvement but also because of the different tunneling rates in each dataset, caused by a shift of the readout point and the 1D nature of the reservoir (see Appendix I).

Further, the fidelity improves as Δt is increases since more $|\uparrow\rangle$ are captured, see Fig. 2(j). However, beyond an optimal value, the fidelity worsens because of the additional opportunities for the background noise to surpass the threshold. Spin mapping errors due to thermal excitation and relaxation are negligible due to their large time constant, being the relaxation time $T_1 = 5.2$ ms and the time constant for a thermal excitation $t_{\text{out}}^\downarrow = 309$ and 70 s without and with the JPA, respectively.

We obtain a maximum spin readout fidelity $F_M = 98.85\%$ without the JPA at $\Delta t = 434 \mu\text{s}$ and $f_{\text{eff,BW}} = 25$ kHz and $F_{M,\text{JPA}} = 99.45\%$ for measurements obtained with a JPA using $\Delta t_{\text{JPA}} = 268 \mu\text{s}$ and $f_{\text{eff,BW}}^{\text{JPA}} = 122$ kHz (see Appendix N for a comparison of fidelities calculated with the same dot-to-reservoir tunneling rates). We note $F_{M,\text{JPA}} = 99\%$ is already achieved at $\Delta t_{\text{JPA}} = 131 \mu\text{s}$. We further explore machine-learning-based approaches to improve readout fidelity [31,32]. Here, by using neural networks, we report an increased fidelity of $F_M = 99.1\%$ in $\Delta t = 500 \mu\text{s}$, and $F_{M,\text{JPA}} = 99.54\%$ in $\Delta t = 250 \mu\text{s}$ without and with a JPA, respectively (see Appendix O for more information).

Finally, we analyze the impact of t_{out}^\uparrow on the readout fidelity. During this period, spin $|\uparrow\rangle$ and $|\downarrow\rangle$ cannot be differentiated adding idle time to Δt . We simulate readout traces with asymmetric tunnel rates $t_{\text{out}}^\uparrow \ll 1 \mu\text{s}$ and $t_{\text{in}}^\downarrow = 228 \mu\text{s}$ and obtain $F_M = 99.3\%$ in just $4 \mu\text{s}$ (see Appendix P for a full discussion). The result shows that the SEB could assign a spin label in much shorter time-scales with equivalent fidelity if a spin-to-charge conversion mechanism with these tunneling characteristics could be used.

IV. PAULI SPIN BLOCKADE

A favorable physical mechanism for single-shot readout is that of Pauli spin blockade based on the large asymmetry in tunnel rates between two spin configurations. In this second demonstration, the device consists of a silicon nanowire transistor with four wraparound gates in series as shown in Fig. 3(a). The QD under gate 1 acts as a SEB with a larger $\alpha = 0.40$ due to the wraparound nature of the gates (see Appendix Q for calculating α , T_e , and γ). It is dispersively measured using an LC lump-element resonator consisting of a 160 ± 5 nH NbN superconducting

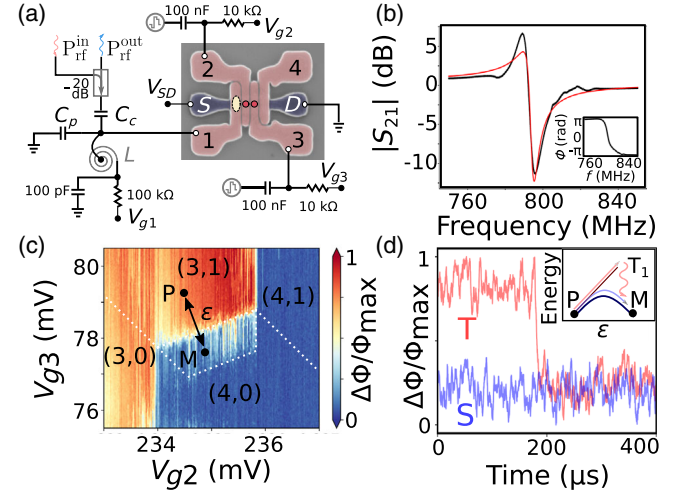


FIG. 3. Experimental setup. (a) False-colored scanning electron micrograph of a silicon nanowire transistor with wraparound gates, under which QDs form. The QD under gate 1 is operated in the many electron regime (yellow ellipse) and acts as a SEB. Gate 1 is connected to a lumped-element resonator probed at a frequency f_r for dispersive readout. The QDs under gates 2 and 3 are charge sensed in the few-electron regime (red circles) and the gates are connected to fast pulse lines for spin manipulation. (b) Resonator response at base temperature. (c) Interdot charge transition (ICT) from (3,1) to (4,0) along which PSB is observed. The points P and M are used, respectively, to prepare and measure or initialize the spin state. (d) Singlet (blue) and triplet (red) exemplary single-shot traces with an energy diagram as an inset showing the energy states close to the (3,1)–(4,0) anticrossing.

TABLE I. Summary of parameters relevant for SEB charge sensing.

Type	Parameter	Elzerman		PSB
		JPA off	JPA on	
Resonator	β	2.5	2.5	1.05
	C_{tot} (fF)	460	460	250
	Q_0	270	270	298
	Z_r (Ω)	520	520	800
	f_r (MHz)	665.5	668	797
SEB	α	0.35	0.35	0.40
	η	1	1	1
	γ (GHz)	70	74	< 4.25
	T_e (mK)	137	137	115
Noise	T_n (K)	2.5	0.25 (0.56 ^a)	2.5
Sensor	τ_m (μ s)	0.45	0.1	0.17
Spin mapping	T_1 (ms)	5	5	0.23
	t_{out} (μ s)	53	31	< 1 ^b
Benchmark	F_M (%)	99.1 ^c	99.54 ^d	99.21
	Δt (μ s)	500 ^c	250 ^d	5.6

^aNoise temperature measured at 665.5 MHz.

^bSinglet tunneling time in PSB.

^cNo neural networks applied 98.85% in 434 μ s.

^dNo neural networks applied 99.45% in 268 μ s.

spiral inductor and a capacitance $C_c + C_p$ of 250 fF [extracted from the natural frequency of the resonator, $f_{\text{rf}} = 797$ MHz, in Fig. 3(b)]. Given the improved matching ($\beta = 1.05$), internal quality factor ($Q_0 = 298$), resonator impedance ($Z_r = 800 \Omega$), and higher frequency, this second implementation of the SEB reaches a $\tau_m = 170$ ns (see Table I and Appendix R for the resonator analysis). We use the SEB to sense the charge state of a few-electron double quantum dot under gates 2 and 3 using a proportional integral derivative (PID) feedback loop [33] (see Appendix S for its implementation). We observe a trapezoidal region in which PSB occurs both in the (1,1)–(2,0) and the (3,1)–(4,0) charge transitions from which we extract a 16 μ eV and 195 μ eV valley and orbital splittings, respectively (see Appendix T for valley-orbit splitting extraction). The larger (3,1)–(4,0) splitting aligns with previous observations in planar devices of an excited state with predominate orbital character [34]. Because of the larger measurement window, we operate in the (3,1)–(4,0) charge transition region, as shown in Fig. 3(c), acquired without feedback. The sensor operates in the strongly sensitive regime (see Appendix U). To determine the readout fidelity, we initialize by waiting at point M for 5.1 ms, such that the system relaxes to the ground state, a singlet (4,0). To prepare a mixed singlet-triplet population, we pulse with a 100 ns ramp to point P and wait for 533 μ s, with a 30 mT magnetic field applied. By pulsing back to

point M, also with a 100 ns ramp, only the singlet is allowed to tunnel, which does so faster than the measurement bandwidth of 1.22 MHz, resulting in a sudden change in charge state. The triplet, being the excited state at point M, needs to relax to the singlet before it can tunnel, resulting in a delayed response of characteristic timescale T_1 . We record the first 400 μ s after the pulse to point M for 10 000 shots, for which we show exemplary traces for both singlet (blue) and triplets (red) in Fig. 3(d).

By plotting the occurrence of average values of each trace for a given measurement time Δt , a bimodal probability distribution associated with the singlet and triplet outcomes appears; see Fig. 4(a) and Appendix V. In this case, the data can be fit to a well-established model for PSB readout that includes Gaussian probabilities for the singlet and triplet outcomes as well as the contribution from triplet decays [35]. From the fitted parameters, we determine the optimum threshold voltage for a maximum visibility of 98.5%, as shown in Fig. 4(b). This data analysis can be carried out as a function of measurement time Δt . In Fig. 4(c), the spin readout infidelity $1 - F_M$ decreases as Δt increases due to a reduction of the measurement noise. However, at longer timescales, triplets start decaying into the (4,0) charge configuration, which decreases the readout fidelity. We find $T_1 = 228.6 \pm 0.5 \mu$ s. Single-shot datasets were taken for varying rf powers, resulting in a maximum fidelity $F_M = 99.21 \pm 0.03\%$ in 5.6 μ s, as shown in Fig. 4(d). From the difference between the sensor-limited readout fidelity [considering $T_1 \rightarrow \infty$ (red crosses)] and F_M (stars), we determine the sources of error for our optimum readout as being 0.63% due to T_1 induced errors and 0.16% due to the sensor.

Finally, we explore the role of temperature. There has been recent interest in operating QDs at elevated temperatures [36,37] due to the additional cooling power that would facilitate the cointegration with classical electronic circuits and the development of an all-silicon quantum computing system [38,39]. We see in Figs. 4(e) and 4(f) that F_M decreases with increasing temperature to $97.39 \pm 0.18\%$ in 23.6 μ s at 530 mK and to $93.90 \pm 0.28\%$ in 27.1 μ s at 1 K. The prevailing factor in the decrease in fidelity is a reduction in the SNR of the SEB charge transition [red dots in Fig. 4(f)] impacting the electrical infidelities [dashed lines in Fig. 4(e)]. This result also explains why the minimum infidelity occurs at higher Δt with respect to base temperature. For $T_{\text{fridge}} \geq 500$ mK, the SNR decreases more rapidly than the expected $1/T_{\text{fridge}}$ dependence [red fit in Fig. 4(f) and see Appendix W] because the charge sensing shift of the SEB becomes smaller than its FWHM, leading to a fractional signal change, $\eta < 1$. Summarizing, sensor-induced errors are responsible for 12.2% of the error at 1 K while T_1 -induced errors are responsible for less than 0.8%; see overhead inset in Fig. 4(f).

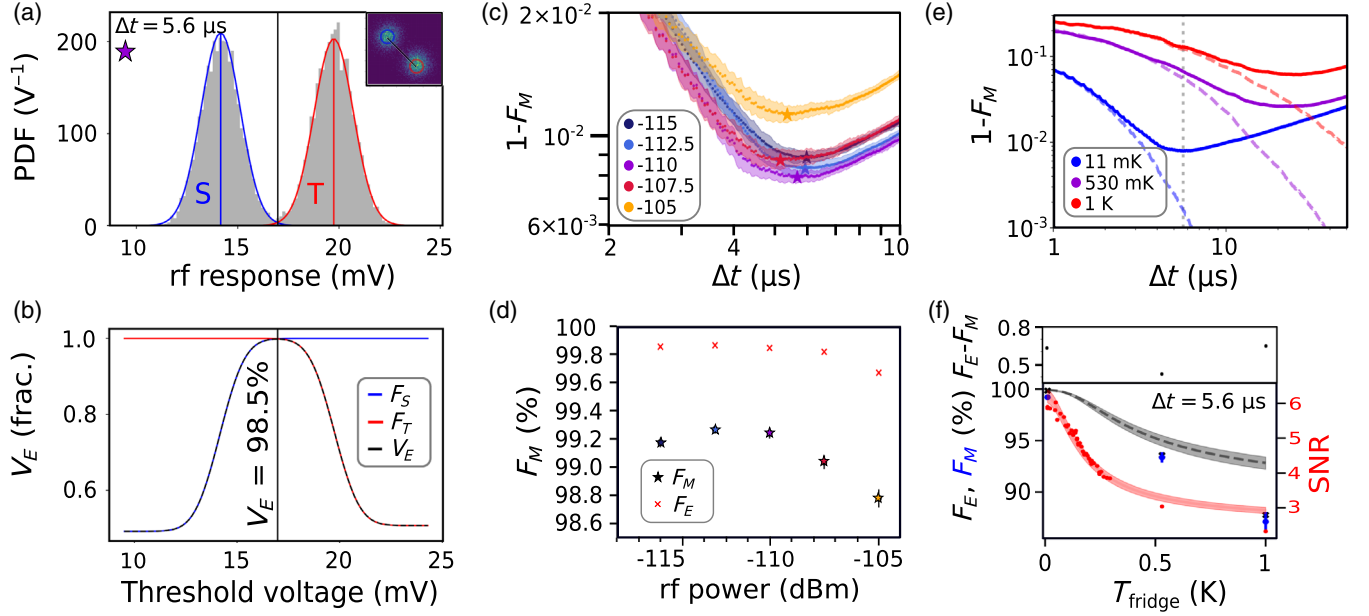


FIG. 4. Spin readout fidelity. Data were acquired with a sampling rate of 20 MHz and a measurement bandwidth of 1.22 MHz. (a) Histogram of 10 000 single-shot measurements averaged over $5.6 \mu\text{s}$ with the fitted distribution of singlets (blue) and triplets (red), according to Ref. [35]. Inset shows the singlet-triplet distribution in the IQ plane, from which the binomial distribution is obtained. (b) Readout visibility V_E as a function of threshold voltage used to discern singlets from triplets. (c) Measurement infidelity ($1 - F_M$) with respect to measurement time Δt for varying rf powers applied to the resonator. (d) Readout fidelity as a function of rf power, reaching an optimum between -112.5 and -110 dBm. The red crosses correspond to the electrical fidelity. (e) Measurement infidelity (solid lines) and electrical infidelity (dashed lines) with respect to measurement time Δt at varying temperatures measured at -110 dBm. The vertical dashed line is at $\Delta t = 5.6 \mu\text{s}$. (f) Measured readout fidelity (blue dots), electrical fidelity (black dots), and SEB signal-to-noise ratio (red dots) as a function of temperature for $\Delta t = 5.6 \mu\text{s}$. The red line is a $(T_e^2 + T_{\text{fridge}}^2)^{-1/2}$ fit to the SNR. The gray dashed line is the associated electrical fidelity, $F_E = \{1 + \text{erf}[\text{SNR}/(2\sqrt{2})]\}/2$. Overhead inset highlighting T_1 -induced errors.

V. DISCUSSION

We have determined that under asymmetric spin tunneling conditions, the two demonstrations would reach fault-tolerant readout fidelity in a few microseconds. These results highlight the benefits of PSB over tunneling to a reservoir but also open the question of how best to design a SEB to achieve faster readout, to go from readout times comparable to the magnetically driven one- and two-qubit gates [40] to the now more common electrically driven ~ 100 ns gate operation times [1–3,41]. To answer this question, we calculate the technological parameters that determine τ_m . In the small signal regime (see Appendix I), the measurement rate can be expressed as

$$\tau_m^{-1} \propto \eta^2 \frac{\beta}{(1 + \beta)^2} \frac{(\alpha e)^2}{k_B T_n} Q_0 Z_r \frac{f_{\text{rf}}^2}{(1 + f_{\text{rf}}^2/\gamma^2)^2}. \quad (3)$$

We find that the charge sensing regime (quantified by η , the fractional change in ΔC due to a charge sensing event), the lever arm, and the operation frequency have the highest impact with a quadratic dependence. However, f_{rf} cannot be increased indefinitely, otherwise electron tunneling to and from the SEB may not occur. Then low-loss, high-impedance resonators close to critical coupling are desired

although τ_m is first-order insensitive to the coupling coefficient near $\beta = 1$. Lastly, quantum-limited amplifiers are advantageous. We note that in the large signal regime, an overcoupled resonator may be favorable [25] as long as the reflected power is within the dynamic range of the JPA. In the context of our two demonstrations, see Table I, the lower noise temperature in the spin-dependent tunneling experiment is compensated by the improved resonator specifications in conjunction with the higher α in the PSB-based demonstration. The wraparound gate design is favorable since it provides a larger gate lever arm. If a JPA were to be used in this instance, τ_m could be further reduced to ≈ 17 ns. Considering this scenario, combined with a longer T_1 (1 ms) to reduce the impact of relaxation, a fidelity of 99.97% in $1.2 \mu\text{s}$ could be achieved, based on the analysis in Ref. [35]. Further improvements can be achieved by using devices with smaller equivalent oxide thickness, and hence larger α [42], and microwave resonators [23,43]. Such modifications could bring the readout time down to a few 100 ns making it comparable with the common gate operation times [3,41].

VI. CONCLUSIONS AND OUTLOOK

We have presented results at the state of the art for spin readout using dispersive charge sensors and demonstrated

high-fidelity readout in timescales much shorter than the coherence time of electron spins in silicon. The reduced footprint of the SEB compared to standard dissipative charge sensors, like the SET, will facilitate the development of highly connected QD-based quantum processors, placing dispersive charge sensing at the forefront of readout methodologies for scalable spin-based quantum processors (see Appendix X for possible architectures).

ACKNOWLEDGMENTS

This research was supported by European Union's Horizon 2020 research and innovation programme under Grant Agreement No. 951852 (QLSI), and by the UK's Engineering and Physical Sciences Research Council (EPSRC) via the Cambridge NanoDTC (EP/L015978/1), CDT in Delivering Quantum Technologies (EP/L015242/1), QUES2T (EP/N015118/1), and the Hub in Quantum Computing and Simulation (EP/T001062/1). V. N. C.-T. is supported by a Telefonica British-Spanish Society scholarship. M. F. G.-Z. is supported by the UKRI Future Leaders Fellow programme (MR/V023284/1). N. S. and J. W. A. R. acknowledge funding from the EPSRC Core-to-Core International Network Grant "Oxide Superspin" (No. EP/P026311/1).

APPENDIX A: SINGLE-ELECTRON BOX OPTIMIZATION

In this appendix, we derive Eq. (3) in the main text. The SNR of the method is defined as

$$\text{SNR} = \frac{\Delta P_{\text{rf}}}{P_n} = |\Delta\Gamma|^2 \frac{P_{\text{in}}}{P_n}, \quad (\text{A1})$$

where $\Delta\Gamma$ is the change in reflection coefficient between the two spin states and $P_{\text{in}(n)}$ is the input (noise) power. In the small signal regime, where the product of the loaded quality factor and fractional change in capacitance is $Q_L \Delta C_D / (2C_{\text{tot}}) \ll 1$, $\Delta\Gamma$ can be calculated as

$$\Delta\Gamma = \Delta C_D \left. \frac{\partial\Gamma}{\partial C_D} \right|_{f_{\text{rf}}=f_{\text{res}}} = i \frac{2\beta}{(1+\beta)^2} Q_0 \frac{\Delta C_D}{C_{\text{tot}}}, \quad (\text{A2})$$

where f_{res} is the natural frequency of oscillation, β is the coupling coefficient, and Q_0 is the internal Q factor [44]. The change in capacitance due to a charge sensing event in the low-power and thermally broadened regime is [16]

$$\Delta C_D = \eta \frac{(\alpha e)^2}{2k_B T_e} \frac{1}{1 + (f_{\text{rf}}/\gamma)^2}, \quad (\text{A3})$$

where η is the fractional change in capacitance due to a charge sensing event (bounded between 0 and 1), α is the gate lever arm, e the charge quantum, k_B the Boltzmann constant, T_e is the electron temperature, and γ is the SEB-reservoir tunnel rate. However, when driven at higher

powers, the maximum value of Eq. (A3) can be reduced due to power broadening effects. In this limit, the capacitance can be calculated following the approach in Ref. [45] that considers the adiabatic limit (where rf-induced excitation and inelastic relaxation processes can be neglected). We find the change in capacitance,

$$\Delta C_D = \eta \frac{2\alpha e}{\pi V_{\text{dev}}} \frac{1}{1 + (f_{\text{rf}}/\gamma)^2} f_c(x), \quad (\text{A4})$$

where V_{dev} is the voltage amplitude of the oscillatory voltage arriving at the gate of the SEB, $x = (\alpha e V_{\text{dev}} / k_B T)$, and f_c is a dimensionless function of the form

$$f_c(x) = \pi f_{\text{rf}} \int_0^{1/f_{\text{rf}}} \frac{\sin(2\pi f_{\text{rf}} t) dt}{1 + \exp[-x \sin(2\pi f_{\text{rf}} t)]}. \quad (\text{A5})$$

which increases monotonically as a function of V_{dev} until it saturates to the value of 1. Next, we calculate the relationship between P_{in} and V_{dev} . For the capacitively coupled parallel LCR resonator used in the main text, we find that

$$P_{\text{in}} = \frac{V_{\text{dev}}^2 (1 + \beta)^2}{R} \frac{1}{4\beta}. \quad (\text{A6})$$

Here R corresponds to the resonator losses, a resistor in parallel with the inductor, parasitic capacitance, and SEB. We then substitute Eqs. (A2), (A4), and (A6) in Eq. (A1) and find Eq. (3) in the main text:

$$\tau_m^{-1} = 32\eta^2 \frac{\beta}{(1+\beta)^2} \frac{(\alpha e)^2}{k_B T_n} Q_0 Z_r \frac{f_{\text{rf}}^2}{[1 + f_{\text{rf}}^2/\gamma^2]} f_c^2(x). \quad (\text{A7})$$

Here we have used $Q_0 = R\sqrt{C_{\text{tot}}/L}$ and defined the loaded resonator impedance $Z_r = \sqrt{L/C_{\text{tot}}}$. Further, we have used $P_n = k_B T_n / (2\tau)$, with τ being the integration time and τ_m the integration time for $\text{SNR} = 1$. We note the noise temperature on the JPA is gain dependent. If the reflected power from the resonator is larger than the 1 dB compression point, the gain drops with a consequent increase in noise temperature.

In the large signal regime, where $Q_L \Delta C_D / (2C_{\text{tot}}) \gtrsim 1$, Eq. (3) is modified as [25]

$$\tau_m^{-1} = \frac{32\eta^2 \frac{\beta}{(1+\beta)^2} \frac{(\alpha e)^2}{k_B T_n} Q_0 Z_r \frac{f_{\text{rf}}^2}{[1 + f_{\text{rf}}^2/\gamma^2]} f_c^2(x)}{[1 + (Q_L \frac{\Delta C_D}{C_{\text{tot}}})^2]}. \quad (\text{A8})$$

This new regime sets an optimal value for the quality factor of the resonator $Q_L = 2C_{\text{tot}}/\Delta C_D$; i.e., the bandwidth of the resonator should be equal to the induced frequency shift by the change in quantum capacitance. Including this consideration in Eq. (A8) and, after some algebra, we arrive to

$$\tau_m^{-1} = 2\eta \frac{\beta}{(1+\beta)} \frac{f_{\text{rf}}}{(1 + f_{\text{rf}}^2/\gamma^2)} \frac{\alpha e V_{\text{dev}}}{k_B T_n f_c(x)}. \quad (\text{A9})$$

We can estimate the measurement rate using some simple assumptions, $\eta = 1$, $\beta \gg 1$, $f_{\text{rf}} \ll \gamma$, $e\alpha V_{\text{dev}} \gg k_B T$, to find

$$\tau_m^{-1} = \frac{2I_g V_{\text{dev}}}{k_B T_n}, \quad (\text{A10})$$

where $I_g = e\alpha f_{\text{rf}}$ is the gate current. Considering some typical values, $\alpha = 0.4$, $f_{\text{rf}} = 1$ GHz, $T_n = 2.5$ K, and $V_{\text{dev}} = 100$ $\mu\text{V} \ll E_c/e$, where E_c is the charging energy, we find $\tau_m^{-1} = 186$ MHz.

We note that the theory used to obtain the measurement rate of the SEB can be easily adapted to dispersive gate readout [23]. For singlet-triplet spin qubits, a singlet outcome has finite quantum capacitance whereas a triplet outcome has zero [14]. Hence the expression for the small signal regime [Eq. (A7)] and large signal regime [Eqs. (A8) and (A9)] can be used for dispersive readout by setting $\eta = 1$. However, there will be an impact of increasing the excitation frequency while providing the optimal driving rf excitation, $e\alpha V_{\text{dev}} \gg 2t_c$, as discussed above. Here t_c is the tunnel coupling energy of the double quantum dot used to implement the singlet-triplet qubit and α is the interdot lever arm. Such a situation may lead to Landau-Zener transitions and Landau-Zener-Stückelberg interference [46] impacting the result of the measurement. As such, we predict the frequency for dispersive gate readout should be kept well below the coupling energy $hf_{\text{rf}} \ll 2t_c$. Alternatively, the coupling energy should be increased to allow a higher probing frequency and hence a larger measurement rate.

APPENDIX B: RADIO-FREQUENCY SINGLE-ELECTRON TRANSISTOR OPTIMIZATION

The single-electron transistor is a resistive charge sensor with single-electron sensitivity and works under the principle that a charge change in its environment is sufficient to produce a sizable change in its bias potential that results in a measurable change in device resistance. Such resistance values can be determined using radio-frequency methods. We model the SET as a variable two-port resistance between the source and drain R_{SET} . We consider the SET to be embedded in the same matching network as the SEB and is placed in parallel with the inductor L and the parasitic capacitance C_p . In this case, at the resonance frequency, the impedance of the resonator and SET is transformed to

$$Z_{\text{eq}} = \frac{L(C_c + C_p)}{C_c^2 R_{\text{SET}}}, \quad (\text{B1})$$

where C_c is the coupling capacitor [42]. As in the case of the SEB, we focus on maximizing the SNR as defined in

Eq. (A1). First, we discuss the conditions under which $|\Delta\Gamma|$ is maximum. We consider that a charge sensing event is capable of shifting the resistance of the SET from its maximum value in the off state to its minimum value in the on state (large signal regime). In the off state, considering $R_{\text{SET}}^{\text{off}} \gg L(C_c + C_p)/(C_c^2 Z_0)$, the reflection coefficient is

$$\Gamma_{\text{off}} = -1. \quad (\text{B2})$$

In the on state, the reflection coefficient is

$$\Gamma_{\text{on}} = \frac{1 - \beta_{\text{on}}}{1 + \beta_{\text{on}}}, \quad (\text{B3})$$

where $\beta = Z_0/Z_{\text{eq}}$ is the coupling coefficient. Overall, the result can be summarized as

$$|\Delta\Gamma| = \Gamma_{\text{on}} - \Gamma_{\text{off}} = \frac{2}{1 + \beta_{\text{on}}}. \quad (\text{B4})$$

Secondly, we consider the limits on P_{in} , the power applied to the resonant circuit. For this calculation, we take into account that the voltage drop at the input of the SET, V_{SET} , has an upper bound limited by the characteristic energy voltage scales of the SET Coulomb oscillations. Using Eq. (A6), we find that

$$P_{\text{in}} = \frac{V_{\text{SET}}^2 (1 + \beta_{\text{on}})^2}{R_{\text{SET}}^{\text{on}} 4\beta_{\text{on}}}. \quad (\text{B5})$$

We can now calculate the signal $S = |\Delta\Gamma|^2 P_{\text{in}}$ using Eqs. (B4) and (B5) and considering a constant power applied (which will be the power in the on state since this will produce the maximum voltage drop at the device):

$$S = \frac{V_{\text{SET}}^2}{\beta_{\text{on}} R_{\text{SET}}^{\text{on}}}. \quad (\text{B6})$$

In the case of critical coupling as commonly considered the most sensitive point of the SET [26], Eq. (B6) can be expanded into a more convenient form,

$$S = \frac{V_{\text{SET}}^2 Z_r^2}{R_{\text{SET}}^{\text{on}^2} Z_0} = I_{\text{on}}^2 \left(\frac{Z_r}{Z_0} \right)^2, \quad (\text{B7})$$

where I_{on} is the amplitude of the ac current through the SET in the on state and $Z_r = \sqrt{L(C_c + C_p)/C_c^2}$. Finally, we calculate the SNR considering two possible scenarios: (i) noise dominated by the HEMT amplifier and (ii) shot-noise limited. In case (i), $P_n = k_B T_n/(2\tau)$, the measurement rate for a SNR = 1 reads

$$\tau_m^{-1} = \frac{2I_{\text{on}}^2}{k_B T_n} \left(\frac{Z_r}{Z_0} \right)^2 = \frac{2I_{\text{on}}^2 R_{\text{set}}^{\text{on}}}{k_B T_n}, \quad (\text{B8})$$

whereas in case (ii), the shot noise power for the SET is

$$P_n = \frac{\sqrt{2}eFI_{\text{on}}R_{\text{SET}}^{\text{on}}}{\tau}, \quad (\text{B9})$$

where F is the Fano factor which accounts for the correlations between charge tunneling events in the SET. Note that I_{on} is the amplitude not the rms current. For a symmetric SET (same value of tunnel resistances), $F = 0.5$. In this case, the measurement rate reads

$$\tau_m^{-1} = \frac{I_{\text{on}}}{\sqrt{2}eF} \left(\frac{Z_r^2}{Z_0 R_{\text{SET}}^{\text{on}}} \right) = \frac{I_{\text{on}}}{\sqrt{2}eF}. \quad (\text{B10})$$

For a comparison with the SEB, it is useful to express Eq. (B8) as

$$\tau_m^{-1} = \frac{2I_{\text{on}}V_{\text{SET}}}{k_B T_n}, \quad (\text{B11})$$

and consider similar typical values $I_{\text{on}} = 1$ nA, $V_{\text{dev}} = 100$ $\mu\text{V} \ll E_c/e$, and $T_n = 2.5$ K, we find $\tau_m^{-1} = 5.80$ GHz. In other words, the ratio between the SET and the SEB measurement rates can be expressed as

$$\Lambda = \frac{\tau_m^{-1}(\text{SET})}{\tau_m^{-1}(\text{SEB})} = \frac{I_{\text{on}}T_n^{\text{SEB}}}{I_g T_n^{\text{SET}}}, \quad (\text{B12})$$

where $T_n^{\text{SEB}(\text{SET})}$ is the noise temperature of the SEB (SET) system, dominated by either the cryogenic amplifier or the intrinsic noise source of the sensor. We observe the measurement rates in both devices are governed by the current that can flow through the system in the sensing configuration and the noise equivalent temperature of the system. Our analysis seems to imply that both the SET and the SEB are embodiments of the same physical process for sensing (electron tunneling).

APPENDIX C: FABRICATION DETAILS

Both devices are MOS transistors fabricated in an industrial cleanroom using 300 mm wafers of 7 nm silicon on insulator with a 145-nm-thick buried oxide. The gate oxide is 6 nm of thermal SiO_2 and the gate metal is 5 nm TiN and 50 nm polycrystalline silicon. Device 1 shown in Fig. 1(a) has four gates on top of the nanowire, two on each side facing each other [see Fig. 1(a)]. The nanowire has a width of $W = 80$ nm and a gate length of $L_G = 50$ nm. The separation between parallel gates is $S_H = 50$ nm, whereas between the gates facing each other is $S_V = 40$ nm. Device 2 shown in Fig. 3(a) has four wrap-around gates in series. The nanowire width is $W = 80$ nm, the gate length $L_G = 50$ nm, and the gate separation is $S_H = 50$ nm. To form the gates, a hybrid deep ultraviolet, electron beam lithography and etching of the gate hard

mask was performed before transferring the dense pattern into the rest of the stack. After gate etching, the nanowire is covered by 34-nm-wide Si_3N_4 spacers. On one hand, the spacer separates the reservoirs from the central part of the intrinsic nanowire, protecting the intrinsic silicon from the posterior ion implantation which defines the reservoirs. And, on the other hand, it also covers the split between the independent gates since the spacer length is larger than half of the intergate gap. The reservoirs are then n doped by arsenic and phosphorus implantation. The process is completed after an activation spike anneal, salicidation (NiPtSi), contacts, and metallization.

In device 1, up to four QDs can be formed on the upper corners of the nanowire, two at each side of the nanowire forming a 2×2 configuration. In device 2, three QDs can be formed in a 1×3 configuration. Gate 4 was not working in this particular demonstration. The dots' electrochemical potential can be controlled by the voltage applied to the gates above them. For further control, the silicon substrate can be used as a backgate and an overarching metal line as a top gate (only in device 1).

APPENDIX D: MEASUREMENT SETUP

Measurements were performed at base temperature of a dilution refrigerator [setup 1 (2) at 15 (11) mK]. dc voltages to the gates and electron reservoirs were delivered through filtered cryogenic loom. In setup 1, the interdot and dot-to-reservoir tunneling rates can be modified by the dc voltage applied to a top metallic gate [20]. The experiments were performed at a constant voltage of $V_{\text{top}} = 7.5$ V applied to the metal line.

The devices' electrodes are connected to the PCB contacts via on-chip aluminium bond wires. On-PCB bias tees are used to combine the dc signals with the radio-frequency signal for gate-based readout and the fast pulses, which are delivered through attenuated and filtered coaxial lines. The bias tee acts on the pulses sent as a high-pass filter. This effect was compensated by pulse engineering using the inverse of the filter transfer function, such that after passing through the bias tee, the pulses had the desired line shape.

The resonator for reflectometry is formed in setup 1 (2) by an 124 ± 4 (160 ± 5) nH NbN planar spiral inductor [42] placed in parallel to the parasitic capacitance to ground of the PCB and the device. It is capacitively coupled to a 50 Ω transmission line via a coupling capacitor 50 (57) fF. The gate connected to the resonator is biased through a low-pass filter on the PCB formed by a 100 k Ω resistor in series with the inductor and a 100 pF capacitor to ground. The PCB is made from 0.8-mm-thick RO4003C with immersion silver finish. On its way out of the fridge, the reflected rf signal is first amplified by 26 dB at 4 K (LNF-LNC0.6_2A) and further amplified at room temperature. Then, the reflected signal magnitude and phase are obtained using quadrature demodulation (Polyphase

AD0540b) and measured using a digitizer in setup 1 (Spectrum M4i.4451-x4) and an oscilloscope in setup 2 (HDO4054A Lecroy). The measurements taken using a JPA have an additional amplification of 16.7 dB at 105 mK [47].

APPENDIX E: RESONATOR PARAMETER EXTRACTION

Here, we show data of our resonator at $B = 0$ T in Fig. 5(a), whose equivalent model is presented in Fig. 5(b). A coupling capacitance C_c connects the transmission line to a parallel configuration of an inductor L , a resistor R_D , representing resonator losses, and a variable capacitance $C_0 = C_p + C_D$, where C_D is the SEB capacitance from its gate and C_p is the parasitic capacitance of the circuit. The equivalent impedance of such resonator is given by [42]

$$Z_L = R_D \frac{j\omega\Delta\omega_0}{\omega_0^2 - \omega^2 + j\omega\Delta\omega_0} + \frac{1}{j\omega C_c}, \quad (\text{E1})$$

where $\Delta\omega_0 = (1/R_D C_0)$ and $\omega_0 = 2\pi f_0 = (1/\sqrt{LC_0})$ are the width and resonant frequency of the unloaded parallel $LR_D C_0$ circuit.

Assuming that R_D does not vary over the range of frequency near the resonance, the real part of the resonator's impedance stays constant, whereas the imaginary part (admittance) passes along different values. Such a behavior corresponds to part of a circle in the complex plane when plotting the reflection coefficient $\Gamma = (Z_L - Z_0)/(Z_L + Z_0)$ at frequencies close to the resonance. The whole circle, so-called resistance circle, has its center on the real axis $\text{Im}\{\Gamma\} = 0$ and crosses it twice: first at the resonant frequency f_r , corresponding to the circle's closest point to the origin, and a second time when the frequency tends to infinity and zero: $f \rightarrow \infty$ and $f \rightarrow 0$, at which $\Gamma = 1$. For an example, see purple scatter circle in Fig. 5(c).

In the case of perfect matching, $\text{Re}\{Z_L\} = Z_0$, the circle is centered at the position $\Gamma = 0.5$ and crosses the origin, leading to $\Gamma = 0$ at f_r . If the resonator is overcoupled ($\text{Re}\{Z_L\} < Z_0 = 50$), the center of the circle is nearer the origin, making its radius larger than 1. In this case, the magnitude of the reflection coefficient $|\Gamma|$ does not tend to zero at the resonant frequency, but its phase $\angle\Gamma$ completes a whole 2π rotation as the frequency is varied across f_r . [See purple scatter in Figs. 5(c)–5(e) for an example of an overcoupled resonator.]

A resistance circle in the complex plane follows a complex Lorentzian scaled and transported from its origin [48,49]:

$$\Gamma = o_c + \left(1 - \frac{2}{1 + j2Q_L\left(\frac{f}{f_r} - 1\right)}\right)r_c. \quad (\text{E2})$$

Here $o_c = (r_L/1 + r_L)$ is the center of the circle, $r_c = (1/1 + r_L)$ is the radius, $r_L = (1/\beta)$ is the real part of the normalized resonator impedance $[(Z_L/Z_0) = r_L + jy_L]$, f_r is the resonant frequency, and Q_L is the loaded quality factor defined as the ratio of the total energy stored in the resonator to the average energy dissipated per cycle multiplied by 2π . If we transport the circle center to the origin, the change in phase is related to the frequency as

$$\phi(\omega) = \theta_0 + 2 \arctan \left[2Q_L \left(1 - \frac{f}{f_r} \right) \right], \quad (\text{E3})$$

where θ_0 is an offset angle. This is considered one of the most accurate ways to obtain the Q factor and resonant frequency of a resonator [49].

Experimentally, the reflection coefficient is extracted by measuring the S parameter S_{21} between the lines driving $P_{\text{rf}}^{\text{in}}$

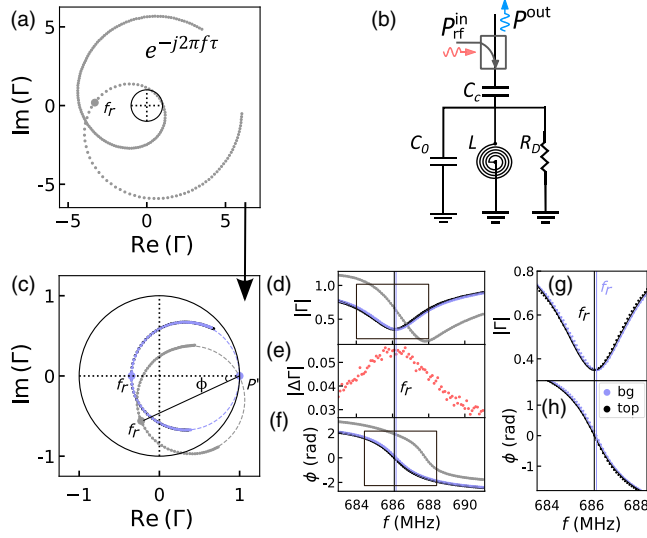


FIG. 5. (a) Γ raw data acquired from a $\sqrt{S_{21}}$ measurement between the ports $P_{\text{rf}}^{\text{in}}$ and $P_{\text{rf}}^{\text{out}}$ shown in (b) for $B = 0$ T. (b) Resonator model including a coupling capacitor (C_c), followed by a resistance (R_D), inductor (L), and a capacitance ($C_0 = C_p + C_D$) in parallel. (c) Measured reflection coefficient and fit before (gray) and after (purple and black) removing the offset angle ϕ . The point of resonant frequency is marked as f_r , whereas the off-resonant point corresponding to $f \rightarrow \infty$ is marked as P' . (d) Absolute value of the reflection coefficient against the frequency, showing that the minimum of the raw data does not correspond to the resonant frequency. (e) Absolute value of the reflection coefficient variation when the SEB is at a charge instability at different frequencies. The maximum variation and, therefore SNR, occurs at f_r . (f) Phase of the reflection coefficient with respect to the frequency. (g),(h) Absolute value and phase of the reflection coefficient on top of a SEB charge transition (top) and out of it (bg) and its respective resonant frequencies shown as vertical lines in their corresponding color. $|\Gamma|$ remains mostly the same, whereas the resonant frequency changes by 70 kHz, revealing that the SEB impedance shift at a charge instability is mostly capacitive.

and $P_{\text{rf}}^{\text{out}}$ with a network analyzer as $\Gamma = \sqrt{S_{21}} = \sqrt{(P_{\text{rf}}^{\text{out}}/P_{\text{rf}}^{\text{in}})}$ [see Fig. 5(a)]. This measurement differs from the expected constant resistance circle due to the effect of the environment leading to [50]

$$S_{21} = ae^{j\alpha}e^{-2\pi jf\tau} \left(1 - \frac{Q_L/|Q_e|e^{j\phi}}{1 + 2iQ_L(f/f_r - 1)} \right). \quad (\text{E4})$$

Here, the constant a takes into account that the amplitude of the outgoing wave has been modified by the attenuators and amplifiers present in the system. Moreover, due to the cable length, the wave has an electrical length characterized by $e^{j\alpha}$ and it acquires a delay τ that makes the phase proportionally dependent on the frequency as $e^{-j2\pi f\tau}$ [50].

Figure 5(c) shows in gray the resonator measured at $B = 0$ T once the effect of the environment has been removed. The additional phase offset ϕ is what produces an asymmetry in the absolute value of the reflection coefficient [see Fig. 5(d)]. Only when the resistance circle is rotated to its right position, the resonant frequency coincides with the minimum in the absolute value of the reflection coefficient [see purple circle in Fig. 5(d)]. The term $e^{j\phi}$ comes from asymmetries of the resonator's transmission signal due to different input and output impedances at the two ports of the resonator [51] or from standing waves in the transmission line connected to the resonator [52]. In order to fit the data to a circle and extract its center and radius, f_r and Q_L , we use a code based on the resonator tools PYTHON library found in Ref. [53].

Figures 5(g) and 5(h) show the magnitude and phase of the reflection coefficient with respect to the frequency at the top of a SEB charge instability (black) and out of it (purple). We found that the resonant frequency is $f_r^{\text{top}} = 686.099 \pm 0.017$ MHz at the charge transition degeneracy point and $f_r^{\text{bg}} = 686.168 \pm 0.016$ MHz away from it. The change in resonant frequency is linked to an increment in the SEB capacitance to ground as $f_r = (1/2\pi\sqrt{L(C_c + C_p + C_D)})$, being the change in capacitance $\Delta C_D = 0.09 \pm 0.03$ fF.

We observed that the system is overcoupled as the phase completes a 2π rotation, but the circle does not cross the origin. The matching, calculated as $\beta = (R/Z_0) > 1$, is barely changed by the SEB, being $\beta^{\text{top}} = 2.064$, $\beta^{\text{bg}} = 2.061$ at and away from the charge degeneracy point, respectively, and neither is the loaded Q factor: $Q_L^{\text{top}} = 125.3 \pm 0.5$ and $Q_L^{\text{bg}} = 125.7 \pm 0.5$. This means that the charge instability in the SEB produces a capacitive change, which we confirm later. Because we are measuring a small change in the device capacitance, the maximum change in $|\Delta\Gamma|$ and, therefore SNR, occurs at the resonant frequency [42], where the slope in phase is maximum [see Fig. 5(e)].

As magnetic field is applied, the kinetic inductance varies, modifying the resonant frequency, Q factor, and

matching. This way, the resonant frequency at $B = 2$ T, at which spin-readout measurements were taken, is $f_r = 665.5$ MHz, the internal Q factor is reduced to $Q_0 = 267$, and the matching is equal to $\beta = 2.5$, as depicted in Fig. 1(a) and summarized in Table I in the main text.

APPENDIX F: JPA CALIBRATION

The JPA used in this experiment consists of a SQUID loop array shunted by a fixed capacitance C_{JPA} [24]. This configuration creates a low quality factor ($Q_{\text{JPA}} < 100$) superconducting resonator, whose resonant frequency f_r^{JPA} can be tuned from 550–750 MHz [see Fig. 6(b)] by passing a current I_{bias} through a nearby coil that modifies the flux through the SQUIDS.

In parametric amplification, one parameter is varied harmonically in a nonlinear medium to create gain. The energy used to modulate the parameter is called the pump. In the case of the JPA, the nonlinearity comes from the

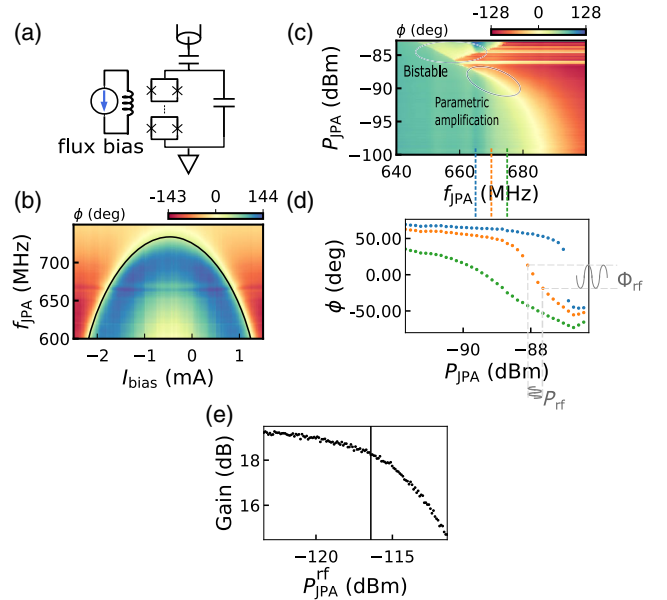


FIG. 6. (a) Sketch of the JPA as a SQUID loop array in parallel with a shunted capacitance connected in reflection to the setup by a coupling capacitance. The magnetic flux generated in a nearby coil by the current I_{bias} is used to tune the JPA's resonant frequency. (b) Reflected phase as a function of the pump frequency and I_{bias} . The resonant frequency is fitted to a function proportional to $\cosh^2(I_{\text{bias}})$. (c) Reflected phase with respect to the pump frequency and the power applied to the JPA. In the region suitable for parametric amplification, the JPA's resonant frequency decreases as P_{JPA} is increased. (d) Amplification transfer function at 3 different frequencies (663 MHz in blue, 668 MHz in orange, and 673 MHz in green). A small variation in the power arriving to the JPA leads to a large variation of the reflected phase, producing a gain. (e) Gain as a function of the rf-probe power arriving to the JPA, for a pump tone of frequency $f_{\text{JPA}} = 665.2$ MHz and power -88 dB. The black vertical line at -116 dBm denotes the rf power for a 1 dB compression in gain.

Josephson junction inductances L_J that are varied harmonically when applying some power P_{JPA} at frequency f_{JPA} (see Fig. 1 of main text). Modifying L_J leads to changes in the JPA's resonant frequency, since $f_r^{\text{JPA}} = (2\pi/\sqrt{C_{\text{JPA}}L_J})$. Figure 6(c) shows the variation of f_r^{JPA} as a function of P_{JPA} . As P_{JPA} increases, f_r^{JPA} is firstly constant, but then it shifts to lower frequencies. Parametric amplification can be achieved in the power range in which f_r^{JPA} varies with respect to P_{JPA} . The JPA amplification transfer function is exemplified in Fig. 6(d), where small variations of the power arriving to the JPA due to the signal tone f_{rf} are translated into large changes in the reflected phase. When the JPA is tuned at even higher pump powers, it becomes bistable [24].

Figure 6(e) shows how increasing the power of the signal tone arriving to the JPA, $P_{\text{JPA}}^{\text{rf}} = P_{\text{rf}}|\Gamma|^2$, leads to a gain reduction, since there is not enough pump energy to be transferred from the pump to the signal and idler. The power at which the gain is compressed by 1 dBm is the JPA's dynamic range (-116 dBm).

APPENDIX G: LEVER ARM AND SEB-TO-RESERVOIR TUNNELING RATES

The lever arm of $\alpha_S = 0.35 \pm 0.06$ is obtained using the slopes of the Coulomb diamonds measured in current [54]. On the other hand, γ can be extracted using the rf response of a SEB electronic transition, which is related to the SEB capacitance ΔC_D (see Fig. 7). In the case that $k_B T < h\gamma$, ΔC_D depends on the electrochemical potential ϵ as $\Delta C_D \propto [h\gamma/\epsilon^2 + (h\gamma)^2]$ [42]. Knowing that $\epsilon = \alpha_S V_S$, we obtain $\gamma = 74 \pm 12$ GHz.

APPENDIX H: SNR CALCULATIONS

To evaluate the readout performance, we send a two-level pulse that varies the IQ (in-phase and quadrature) response between the top of the dot-to-reservoir transition (DRT) and the background [marked with red dots in Fig. 8(a)]. A histogram of the pulse rf response in the quadrature plane shows two separated circular distributions,

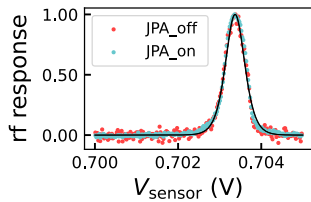


FIG. 7. Normalized rf response from a SEB as a function of the voltage applied to its gate obtained using a low rf-tone power, $P_{\text{rf}} = -91$ dBm. The width of the transition is related to the SEB-to-reservoir tunneling rate, leading to an upper limit of $\gamma \leq 74 \pm 12$ GHz. The same result is obtained with and without a JPA.

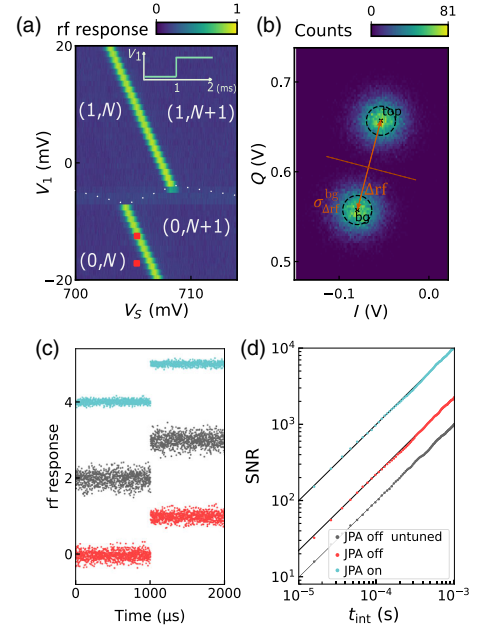


FIG. 8. SNR. (a) Normalized rf response showing the stability diagram of the SEB versus *dot* where the occupation of the SEB and dot is displayed as (dot, SEB). Because of their cross capacitance, the rf response has a shift in voltage when an electron is added to dot. The inset shows the pulses sent to dot to jump on and off the dot-to-reservoir transition, which corresponds with the red points. (b) IQ histogram from 1000 data traces collected by pulsing between the red points marked in (a). The histogram shows two distinct distributions corresponding to the background and the top of the SEB charge instability for data taken without a JPA. The signal is collapsed into 1D using the axis between the center of the so-called Fresnel lollipops. (c) Normalized rf response in the 1D projection for JPA on, off, and optimized JPA off for a measurement bandwidth $f_{\text{eff,BW}} = 12$ kHz. (d) SNR as a function of the integration time.

each one corresponding to the top and background of the DRT [see Fig. 8(b)].

Since the noise is Gaussian and equal in every direction, most of the information is in the axis that joins the centers of the so-called Fresnel lollipops, whereas its perpendicular axis carries just noise. Therefore, we project our data on the optimal axis and use the SNR definition $\text{SNR} = [\Delta \text{rf}^2 / (\sigma_0^2 + \sigma_1^2) / 2]$, where Δrf is the distance between the lollipop centers and $\sigma_{0(1)}$ is the one-dimensional standard deviation of the background (peak).

Figure 8(d) shows SNR as a function of integration time with the JPA off tuned at its optimal point (red), JPA on (blue) and JPA off with the same settings used for the JPA on (gray). Using an extrapolation (black straight lines) we infer the integration time to have a $\text{SNR} = 1$. These times are $\tau_m^{\text{off tuned}} = 451.1 \pm 0.1$ ns, $\tau_m^{\text{off}} = 1.015 \pm 0.001$ μ s, $\tau_m^{\text{on}} = 100.2 \pm 0.8$ ns. This way, the noise temperature is reduced by a factor of $\times 10$ when switching the JPA on. However, the frequency at which this is achieved is not the optimal frequency, i.e., the natural frequency of the

oscillator. The SNR when the JPA is off can be improved by a factor of $\times 4.5$ by choosing the optimal f_{rf} as it is shown in Fig. 1 in the main text. This is a consequence of the higher reflected power at f_r that partially saturates the JPA reducing its gain.

APPENDIX I: ELECTRON TEMPERATURE AND THERMAL EXCITATIONS

Figures 9(a)–9(c) show different situations depending on the voltage applied to the *dot* at the readout stage V_1 . At high voltages, the electron stays in dot [Fig. 9(a)], corresponding to a constant rf response equal to zero, as shown in Fig. 9(d). As the voltage is decreased, the $|\uparrow\rangle$ and $|\downarrow\rangle$ states straddle the reservoir Fermi energy, leading to the transitory behavior in the rf response that allows us to determine whether the electron had a spin up or spin down [see Fig. 9(e)].

At even lower voltages, the electron leaves the dot during the readout stage independently of its spin polarization [Fig. 9(e)]. At this voltage range, we observe the

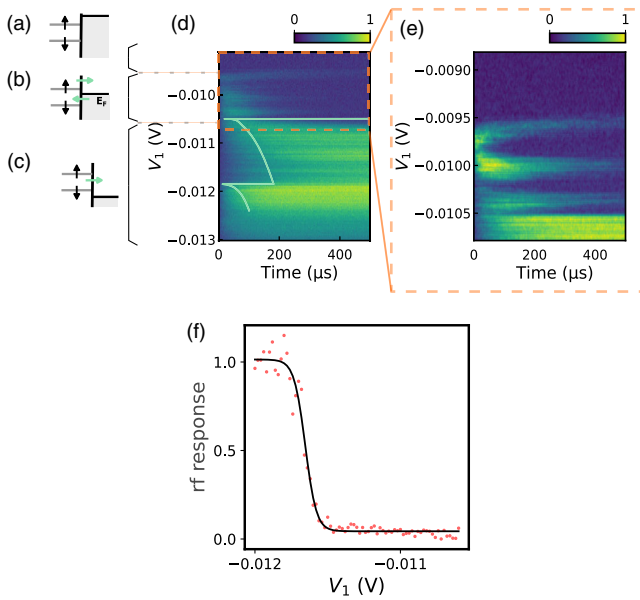


FIG. 9. (a)–(c) Diagrams of dot electrochemical potential with respect to the lead Fermi energy at different voltages applied to the dot gate V_1 . (d) Time-averaged and normalized rf response over time at different V_1 . At the voltages described by the situation in (c), any loaded electron tunnels out during the readout stage. This situation results first in a low value of the rf signal that then increases over time as the electron leaves the dot. The superposed green line is the calculated tunneling times from a quasi-1D reservoir to a 0D dot. At higher V_1 , we encounter the situation pictured in (b), where the reservoir Fermi energy is in between the dot spin $|\uparrow\rangle$ and $|\downarrow\rangle$. This regime is shown with more detail in (e), where we can observe how the quasi-1D density of states from the lead shape the dependency of $t_{\text{out}}^{\uparrow}$ and $t_{\text{in}}^{\downarrow}$ with respect to V_1 . (f) rf response after the transient with respect to V_1 , following a Fermi-Dirac distribution.

characteristic features of tunneling between a zero-dimensional and a one-dimensional system, where the tunneling rate depends on the energy as $\Gamma \propto (1/\sqrt{E - E_n})$, with E_n the position in energy of the reservoir 1D subbands. The simulated tunneling time as a function of V_1 is superposed over the 2D map in Fig. 9(d) with a green line. Around the Fermi level, the reservoir density of states follows a Fermi-Dirac distribution, so that the tunneling rate is a combination of the 1D subbands and the Fermi-Dirac distribution:

$$\Gamma(E) = \frac{2\pi}{\hbar} |\Gamma_0| \left(\sum_n \frac{1}{\sqrt{E - E_n}} \right) [1 - f(E - E_{\downarrow})]. \quad (\text{I1})$$

Here $E = -|e|\alpha_1 V_1$, where α_1 is the lever arm of the gate over dot and e is the electronic charge. $1 - f(E - E_{\downarrow})$ is the distribution of empty states in dot, which is tracked by the rf response after the transient tunneling. The electronic temperature, $T_e = 137 \pm 18$ mK, is extracted by fitting the rf response as a function of V_1 to the Fermi-Dirac distribution [see Fig. 9(f)].

We use the calculated Fermi distribution to obtain the thermal excitation time constant $t_{\text{out}}^{\downarrow}$ at the readout position as $t_{\text{out}}^{\downarrow} = t_{\text{in}}^{\downarrow} \{ [1 - f(E_{\text{readout}} - E_{\downarrow})] / f(E_{\text{readout}} - E_{\downarrow}) \}$ (see Appendix K for more information about $t_{\text{in}}^{\downarrow}$). We obtain a $t_{\text{out}}^{\downarrow} = 309$ s and $t_{\text{out,JPA}}^{\downarrow} = 70$ s for measurements taken without and with a JPA, respectively.

APPENDIX J: EXPERIMENTAL BANDWIDTH

The bandwidth of our experiment is limited by the resonator bandwidth: $(f_r/Q_L) = 6.18 \pm 0.04$ MHz. However, if the signal's frequency components are lower than the resonator bandwidth, a low-pass filter can be introduced to reduce high frequency noise, improving the SNR.

To characterize the measurement bandwidth, we can obtain the effective noise bandwidth as

$$\omega_{\text{eff,BW}} = \int_0^{\infty} \left| \frac{H(j\omega)}{H_{\text{max}}} \right|^2 d\omega, \quad (\text{J1})$$

which corresponds to the bandwidth of a brickwall filter that produces the same integrated noise power. Here, $H(j\omega)$ is the filter transfer function and H_{max} is its maximum.

In this experiment, we used a (minicircuits BLP-1.9+) low-pass filter, whose transfer function was obtained from its insertion loss provided by the manufacturer as

$$\text{insertion loss (dB)} = 10 \log_{10} \left| \frac{V_i}{V_f} \right|^2 = -20 \log_{10} |H_{\text{MC}}(j\omega)|, \quad (\text{J2})$$

where V_i and V_f are the filter's input and output voltage, respectively.

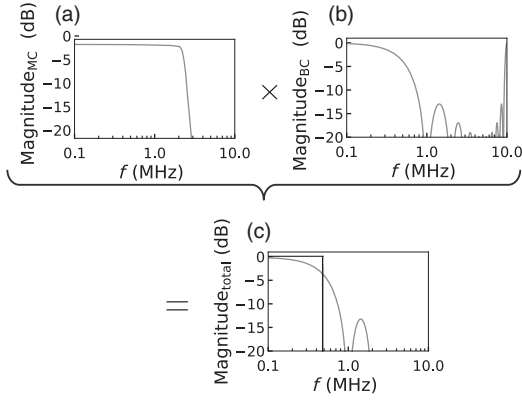


FIG. 10. (a) Bode diagram of the magnitude of the eighth-order minicircuits BLP-1.9+ filter utilized in our measurements. (b) Same for the boxcar filter used to downsample the sample rate from 10 to 1 MHz. (c) Combination of the effects from both filters and equivalent brickwall filter with the same integrated noise power, showing an effective noise bandwidth of $f_{\text{eff,BW}} = 0.49$ MHz.

After that filter, a digital boxcar filter that averages every ten points ($N = 10$) is applied, followed by a decimation process, to reduce the sample rate from 10 to 1 MHz. This way, the total transfer function is equal to $|H_{\text{total}}(j\omega)| = |H_{\text{MC}}(j\omega)H_{\text{BC}}(j\omega)|$, leading to the filter depicted in Fig. 10, with an effective noise bandwidth of $f_{\text{eff,BW}} = (\omega_{\text{eff,BW}}/2\pi) = 0.49$ MHz.

On top of that, some of our measurements include a rolling average filter that takes the average of every N points recursively. This additional filter modifies the total transfer function as $|H_{\text{total}}(j\omega)| = |H_{\text{MC}}(j\omega)H_{\text{BC}}(j\omega)H_{\text{RF}}(j\omega)|$, where $H_{\text{RF}}(j\omega)$ is the rolling average transfer function (see Appendix 1 for more information).

APPENDIX K: PARAMETER EXTRACTION

The electrical fidelity for spin-dependent measurements is calculated by simulating single-shot histograms as the ones shown in Figs. 2(b) and 2(c). In order to create them, we need to reproduce single-shot traces equivalent to the ones measured. An example of a spin $|\uparrow\rangle$ trace is depicted in Fig. 13(a) with a blip starting at $t_{\text{out}}^{\uparrow}$, lasting for $t_{\text{in}}^{\downarrow}$. The background and blip have values $E(\text{low})$ and $E(\text{high})$, with its respective noise, σ_{low} and σ_{high} . This example can be labeled as a spin $|\uparrow\rangle$ trace since it surpasses the threshold voltage V_T .

The experimental parameters that ultimately determine those traces can be separated into the ones that depend on the sensor and the ones that depend on the measured dot. The sensor parameters are independent of the readout method and are the rf response at the background, $E(\text{low})$, and at the blip, $E(\text{high})$, and their respective noise level.

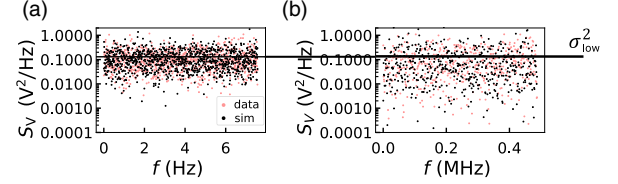


FIG. 11. Noise spectral density of the rf response at $E(\text{low})$ at low frequencies (a) and high frequencies (b) for the acquired data (pink) and the simulations created with Gaussian noise (black).

In order to extract these parameters, 10 000 single-shot spin readout traces like the one displayed in Fig. 13(a) were registered. The average of the rf response at the blip and at the background are equal to the expectation values $E(\text{high})$ and $E(\text{low})$, respectively. To characterize the noise level of the background, we obtain the noise spectral density $S_V(f)$ of the rf response [see Figs. 11(a) and 11(b)]. For lower frequencies, the background noise spectral density is obtained using the last data point of all the consecutive readout traces [see Fig. 11(a)], whereas for higher frequencies we calculate S_V of a single spin $|\downarrow\rangle$ trace [see Fig. 11(b)]. Comparing the noise spectrum with the one generated by a Gaussian random number generator, we concluded that the noise of the background has a Gaussian profile with variance σ_{low}^2 for the whole set of measurements.

The noise at $E(\text{high})$ can include additional sources of noise such as charge noise, where the noise spectral density typically depends on the frequency as $1/f$. This noise originated from the collective behavior of defects or charge traps that act as charge fluctuators as they trap and release electrons [55]. The charge fluctuations slightly modify the potential around the sensor modifying its bias point, so that their effect is more noticeable at the slope of a SEB electronic transition than at the top. Figure 12(a) shows the SEB dot-to-reservoir transition as a function of the voltage applied to dot, where the signal at each point has been

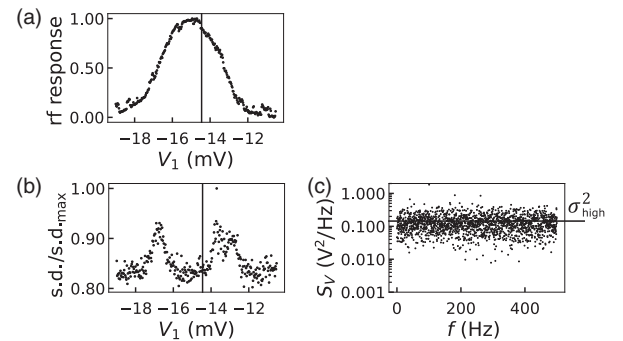


FIG. 12. (a) Average of the normalized rf response for a SEB electronic transition with respect to the voltage applied to the dot gate V_1 . The vertical line indicates the voltage for spin readout. (b) Standard deviation over 2 ms of rf response at $E(\text{high})$ at different voltages. (c) S_V at the blip.

averaged over 2 ms. Figure 12(b) displays their corresponding standard deviations. It is very clear how the standard deviation is higher on the slope than on the offset and top of the peak.

We observe that the readout position—marked as a black vertical line—is at the maximum of the rf response. This has two benefits: on one hand, the contrast between dot empty and occupied is maximum [$E(\text{low})$ and $E(\text{high})$], and, on the other hand, the charge noise is minimized. Figure 12(c) shows that the noise spectral density at the top of the rf response is also constant over the range of frequencies with a variance σ_{high}^2 very similar to σ_{low}^2 .

The rest of the parameters (t_{out}^\uparrow , t_{in}^\downarrow , and A) are set by dot. t_{out}^\uparrow is the time constant for a spin $|\uparrow\rangle$ electron to leave the dot. Such time corresponds with the start time of the blip and can be determined as the time at which the rf response reaches a certain threshold voltage V_T . Registering the number of times that the rf response exceeds such threshold voltage at a given readout time follows an exponential trend whose time constant is t_{out}^\uparrow . t_{in}^\downarrow is obtained following a similar analysis, where the blip duration probability is fitted to an exponential function [see Figs. 13(b) and 13(c)].

The simulated traces for a spin $|\downarrow\rangle$ were created as a set of points with a sample rate of $\Gamma_s = 1$ MHz (as the one of the experiment) and constant value $E(\text{low})$ to which it is added a Gaussian noise characterized by σ_{low} . Spin $|\uparrow\rangle$ traces are generated as a constant value $E(\text{low})$ with Gaussian noise σ_{low} and a blip with a constant value of $E(\text{high})$ and a standard deviation of σ_{high} . The blip starting time and duration follow exponential distributions with time constant t_{out}^\uparrow and t_{in}^\downarrow , respectively.

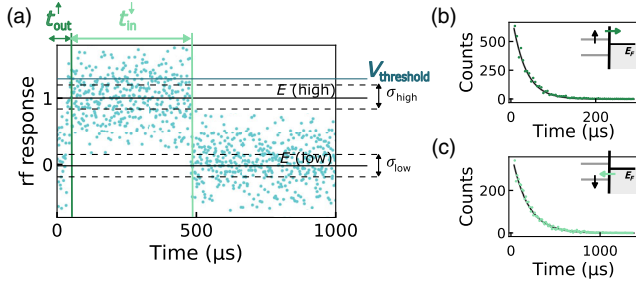


FIG. 13. (a) Normalized rf response of a spin $|\uparrow\rangle$ data trace taken with a JPA using a sample rate of $f_s = 1$ MHz and a measurement bandwidth of $f_{\text{eff,BW}} = 0.49$ MHz. The blip starts when the spin $|\uparrow\rangle$ electron leaves the dot at t_{out}^\uparrow and lasts until a spin $|\downarrow\rangle$ electron replaces it (t_{in}^\downarrow). When dot is occupied the rf response has an estimated value $E(\text{low})$ with a standard deviation σ_{low} , whereas when it is empty the estimated value and standard deviation are $E(\text{high})$ and σ_{high} , respectively. We have also indicated the $V_{\text{threshold}}$ above which the trace is labeled as a spin $|\uparrow\rangle$. (b) Histogram of the starting point of the pulse and exponential fit. (c) Histogram of the pulse duration and fit.

1. Moving average filter

The SNR can be increased in postprocessing by adding an additional low-pass filter, which removes high frequency noise at the price of affecting the blip shape when the cutoff frequency is too low. From the many digital filters available, we used the rolling average filter which takes the average over N points recursively. The first point of the filtered signal corresponds to the mean of the first N points from the original signal and the subsequent points are obtained by shifting forward by one time step the subset of N points that are averaged. Although the rolling average has a complicated frequency dependence [see Fig. 10(b)], it is ideal for this application since it has one of the lowest computation times and is optimal for reducing random noise while retaining a sharp step response [56]. This way, we can test which measurement bandwidth maximizes the readout fidelity with a low computation overhead.

APPENDIX L: MEASUREMENT FIDELITY

The probability of correctly recognizing a spin $|\uparrow\rangle$ electron F_M^\uparrow is given by the sum of the probability that such electron truthfully generates a spin $|\uparrow\rangle$, F_{STC}^\uparrow , and the sensor detects the corresponding blip, F_E^\uparrow , plus the probability of generating a false spin $|\downarrow\rangle$ trace, $1 - F_{\text{STC}}^\uparrow$, that is misidentified as a spin $|\uparrow\rangle$ electron, $1 - F_E^\downarrow$. This way,

$$F_M^\uparrow = F_{\text{STC}}^\uparrow F_E^\uparrow + (1 - F_{\text{STC}}^\uparrow)(1 - F_E^\downarrow). \quad (\text{L1})$$

Equivalently, the probability of correctly recognizing a spin $|\downarrow\rangle$ electron is

$$F_M^\downarrow = F_{\text{STC}}^\downarrow F_E^\downarrow + (1 - F_{\text{STC}}^\downarrow)(1 - F_E^\uparrow). \quad (\text{L2})$$

Both independent fidelities can be combined as

$$F_M = \frac{F_M^\downarrow + F_M^\uparrow}{2} \quad (\text{L3})$$

to calculate the overall measurement fidelity. The electrical fidelity is calculated via Monte Carlo simulations as described in Appendix K, whereas F_{STC} fidelity uses an analytic expression to take into account the errors coming from relaxation and thermal processes. The probability of not having a thermal excitation, so a spin $|\downarrow\rangle$ does not produce a false spin $|\uparrow\rangle$ trace, is given by

$$F_{\text{STC}}^\downarrow = e^{-t/t_{\text{out}}^\downarrow}. \quad (\text{L4})$$

The other infidelity source is the relaxation process of a spin $|\uparrow\rangle$ electron that has not tunneled out of the dot. That can be calculated as the conditional probability $P(A|B)$, being $P(A) = 1 - e^{-t/T_1}$ the probability that a spin $|\uparrow\rangle$ has decayed at time t , and $P(B) = e^{-t/t_{\text{out}}^\uparrow}$, the probability that

an electron with spin $|\uparrow\rangle$ has not left the dot at time t . Since both events are independent, the probability of having a false spin $|\downarrow\rangle$ trace due to a relaxation process is

$$P(A|B) = \frac{P(A \cap B)}{P(B)} = \frac{P(A)P(B)}{P(B)} = P(A) = 1 - e^{-t/T_1}, \quad (\text{L5})$$

Therefore, the probability of not having a relaxation process is e^{-t/T_1} . To calculate the fidelity, we have to add the probability that a spin $|\uparrow\rangle$ relaxes and, subsequently, the spin $|\downarrow\rangle$ electron tunnels down the dot:

$$F_{\text{STC}}^{\uparrow} = e^{-t/T_1} + (1 - e^{-t/T_1})(1 - e^{-t/t_{\text{out}}^{\downarrow}}). \quad (\text{L6})$$

Here, the relaxation time T_1 depends on the magnetic field applied [57], which in this experiment was 5.1 ± 0.4 s, at $B = 2$ T. On the other hand, $t_{\text{out}}^{\downarrow}$ depends on the temperature and the difference in energy between the spin $|\downarrow\rangle$ and the reservoir Fermi energy at the readout stage.

APPENDIX M: F_M DEPENDENCE ON Δt AND MEASUREMENT BANDWIDTH

Here, we investigate the dependence of the measurement fidelity F_M with respect to the measurement bandwidth and the readout time with and without a JPA. On one hand, decreasing the measurement bandwidth improves the SNR, but, on the other hand, it deforms the blip shape, rounding its edges and decreasing its maximum. Figures 14(a) and 14(b) show how decreasing the measurement bandwidth increases the fidelity up to an optimal point. The difference in the optimal measurement bandwidth is due to two different reasons. First, the measurements taken without a JPA have a lower SNR. So, the limiting factor to increase the fidelity is the noisy spin $|\downarrow\rangle$ traces reaching above the threshold. The second reason is that the tunneling rates measured for each setup were slightly different: the blips have a standard duration of $t_{\text{in}}^{\downarrow} = 440$ μs without a JPA and $t_{\text{in,JPA}}^{\downarrow} = 186$ μs . So, the optimal measurement

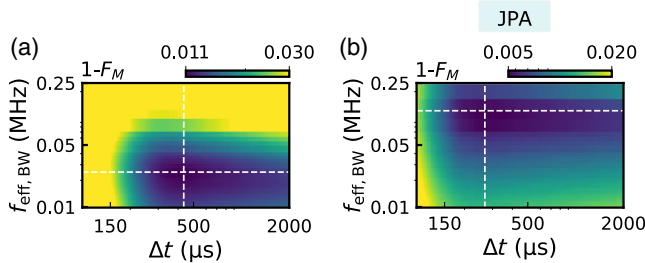


FIG. 14. (a) Dependence of the measurement infidelity $1 - F_M$, with respect to the measurement bandwidth and the readout time. The dashed white lines pass through the maximum fidelity point. (b) Same for measurements taken using JPA.

bandwidth is higher for the set of measurements without a JPA.

F_M also increases with Δt , since more blips can be captured as the readout time duration is longer. However, once the readout time is longer than the standard duration of the spin-dependent tunneling process, the rest of the trace can only lead to errors. For this reason, the optimal readout time with a JPA is shorter, having faster tunneling times $t_{\text{out,JPA}}^{\uparrow}$ and $t_{\text{in,JPA}}^{\downarrow}$. The white dashed lines in Fig. 14 pass through the maximum in F_M and correspond with the 1D plots presented in Figs. 2(c) and 2(d) in the main text.

APPENDIX N: F_M DEPENDENCE ON THE DOT-RESERVOIR TUNNELING RATES

For a direct comparison of fidelities, we calculate the readout fidelity with and without the JPA, using simulated readout traces created with the same tunneling rates ($t_{\text{out}}^{\uparrow} = 53$ μs and $t_{\text{in}}^{\downarrow} = 440$ μs), obtaining $F_M = 98.85\%$ and $F_{M,\text{JPA}} = 99.75\%$, with the JPA off and on, respectively. The readout time is $\Delta t = 434$ μs in both cases, as it maximizes the fidelity for measurements taken without a JPA.

APPENDIX O: MACHINE LEARNING SPIN LABELING APPROACH

The main text describes how to obtain the electrical fidelity using the probability density function of the rf response peak values [Eq. (3)]. However, when applying other spin identification methods, the fidelity can be calculated with an equivalent method that relies on the number of simulated traces wrongly identified:

$$F_E^{\uparrow} = 1 - n_{\uparrow}^0 / N_{\text{tot}}, \quad F_E^{\downarrow} = 1 - n_{\downarrow}^1 / N_{\text{tot}}. \quad (\text{O1})$$

Here, n_{\uparrow}^0 is the number of spin $|\uparrow\rangle$ traces misidentified as $|\downarrow\rangle$ traces, and the opposite holds for n_{\downarrow}^1 . We use this method to calculate the measurement fidelity when using a neural network method to label the readout traces.

The neural network method is summarized in Fig. 15(a). It uses the deep learning architecture known as inceptionTime, a state-of-the-art approach to time series classification. The inceptionTime network involves a series of convolutional layers which apply learned filters to the time series to extract its features [58]. The features extracted from Fig. 15(b) spin traces are shown in Fig. 15(c). These features are fed into a fully connected or dense layer which assigns one of two classes to the input time series (spin up or down). The network was trained using the same body of data that the thresholding method described in the main text, with it divided into training, validation, and test sets. The training set is used to train the model via gradient descent and the validation set is monitored during training to avoid overfitting. If the

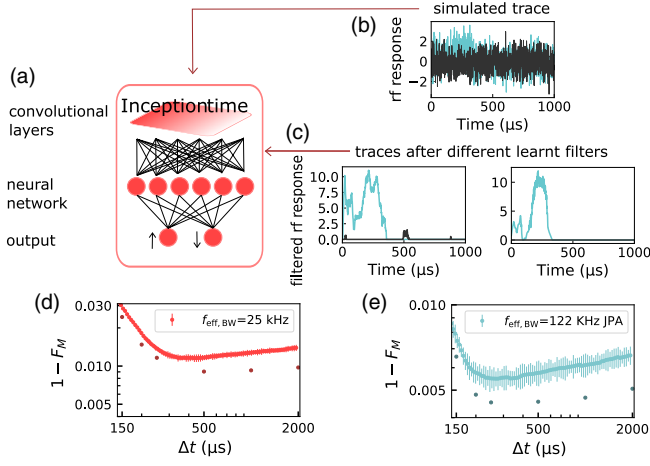


FIG. 15. (a) Working protocol of the machine learning spin-classification approach. (b) Simulated spin $|\uparrow\rangle$ and $|\downarrow\rangle$ trace using the parameters for JPA on. (c) Output of the inceptionTime convolution layers with the blip edges enhanced to facilitate trace classification. (d) Measurement fidelity without a JPA using the threshold method approach (light red) and the machine learning approach (dark red). (e) Same for measurements using a JPA, with the threshold (light blue) and machine learning (dark blue) labeling methods. The error bars for the machine learning method are too small to be visible.

network learns to recognize the training set too well, then that can compromise its performance on unseen data. The network that produces the best validation accuracy is selected and applied to the test set, which gives the final accuracy data reported here. The approach used here uses the `TSAI` package for instantiating the networks and records training metrics using the `Weights and Biases` library, which is also used for hyperparameter optimization [59,60].

Figures 15(d) and 15(e) show an improvement of the fidelity for measurements taken with and without a JPA. Here, the spin to charge errors are also included as described in Appendix L. We find a maximum fidelity $F_M = 99.1\%$ for $\Delta t = 500 \mu\text{s}$ without using a JPA and $F_M^{\text{JPA}} = 99.54\%$ with a JPA for $\Delta t_{\text{JPA}} = 250 \mu\text{s}$. We observed that, when using the machine learning classification method, the measurement fidelity stays almost constant as the readout time Δt increases. This is because the optimized filters enhance the blip's edges features, mitigating the errors that appeared in the threshold method when the background noise surpasses the threshold.

For a fair comparison between the classification methods, we have calculated the accuracy in the fidelity for each method [see error bars in Figs. 15(d) and 15(e)]. To do so, we have assumed that the experimental parameters have no error and used the same simulated set of readout traces.

The fidelity error is calculated based on k -fold validation—we train the neural network on different sections of the dataset and predict the fidelity on the

remaining sections. In the case of the threshold method approach, a set of 1×10^6 simulated traces is divided into 100 subsets of data, each one of equal size. Then, we obtain the optimal threshold for all the subsets except one and obtain the fidelity on the remaining subset. This way, we obtain a different fidelity for each subset. The final fidelity is calculated as the average of the different results and its error as their standard deviation.

For the JPA on, we obtain a fidelity of $99.45 \pm 0.05\%$ with the threshold method and $99.54 \pm 0.002\%$ using machine learning. We then compare these two different fidelity distributions with the Welch's t-test. The t-test result was $p \ll 0.05$. So, we can affirm that both populations can be well distinguished and the change in the fidelity using different classification methods is significant.

APPENDIX P: MEASUREMENT FIDELITY FOR ASYMMETRIC TUNNELING RATES

The readout time for spin-dependent tunneling is limited by the time that a spin $|\uparrow\rangle$ electron takes to leave the dot, $t_{\text{out}}^{\uparrow}$, since until the start of the blip there is no difference between a spin $|\uparrow\rangle$ and $|\downarrow\rangle$ trace. Here, we investigate the measurement fidelity for asymmetric tunneling rates—a fast $t_{\text{out}}^{\uparrow}$, while $t_{\text{in}}^{\downarrow}$ remains long—to reduce the readout time necessary to achieve a fidelity above 99%. These kinds of traces are shown in Fig. 16(a) and are very similar to the ones described in Fig. 3(d) in the main text, showing singlet and triplet traces.

We can make a parallelism between the traces generated using spin-dependent tunneling and Pauli spin blockade. In both cases, the value of the rf response depends on the dot occupation. In the case of PSB, the rf response is maximum for (4,0) and minimum for (3,1), whereas for spin-dependent tunneling it is maximum when the dot is empty and minimum when it has an electron. This way, both singlet and spin $|\downarrow\rangle$ traces are characterized by a constant rf response. On the other hand, a $|\uparrow\rangle$ trace has a blip that starts when the electron leaves the dot, $t_{\text{out}}^{\uparrow}$, and

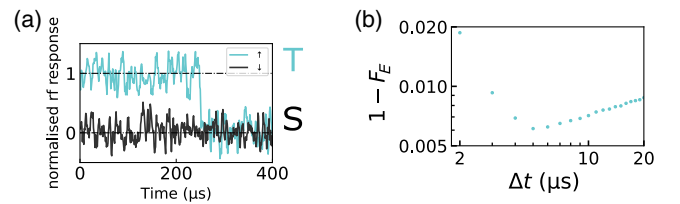


FIG. 16. (a) Spin $|\uparrow\rangle$ and $|\downarrow\rangle$ traces simulated using the experimental parameters of measurements taken with a JPA, with the exception of $t_{\text{out}}^{\uparrow}$ and $t_{\text{in}}^{\downarrow}$ that are modified to emulate triplets and singlets. The spin $|\uparrow\rangle$ is equivalent to a triple trace and, in the same way, the spin $|\downarrow\rangle$ is equivalent to a singlet trace. The traces shown have a measurement bandwidth of $f_{\text{eff,BW}} = 122 \text{ kHz}$. (b) $1 - F_E$ as a function of the readout time.

lasts until a new electron tunnels back from the reservoir to the spin $|\downarrow\rangle$ state, $t_{\text{in}}^{\downarrow}$. In the case of a triplet trace, the blip starts when the system tunnels from the preparation stage, with an occupation of (4,0), to the readout stage, with occupation (3,1). Therefore, a triplet trace starts at a high value that continues until the triplet relaxes to the singlet, characterized by the relaxation time T_1 . To obtain the fidelity, we create traces in the same way described in Appendix K and using the same experimental values extracted for measurements taken with a JPA [$E(\text{high})$, $E(\text{low})$, σ_{high} , σ_{low} , Γ_s , and proportion of spin $|\downarrow\rangle$, A]. However, the tunneling rates are modified in order to emulate triplet or singlet traces. We chose $t_{\text{out}}^{\uparrow} = 0.01 \mu\text{s}$ and $t_{\text{in}}^{\downarrow} = 228 \mu\text{s}$, so that $t_{\text{in}}^{\downarrow}$ is equal to the triplet relaxation time T_1 from the Pauli spin blockade experiment described in the main text.

The average of the trace during Δt is compared against a threshold, which is varied to obtain the maximum fidelity. Figure 16(b) has the fidelity at different readout times Δt . We obtain a maximum $F_E = 99.3\%$ for a readout time $\Delta t = 4 \mu\text{s}$.

APPENDIX Q: LEAVER ARM, ELECTRON TEMPERATURE, AND TUNNEL RATE OF THE SEB

To determine the lever arm α of the SEB, we carried out a magnetospectroscopy measurement of the SEB dot-to-reservoir line close to the interdot charge transition (ICT) of interest, as shown in Fig. 17(a). From the analysis carried out in Appendix U, and due to the linear dependence of the magnetospectroscopy, the transition is temperature broadened and thus the phase response $\Delta\Phi$ takes the form

$$\Delta\Phi \propto \frac{1}{\cosh^2\left(\frac{\alpha(V_{g1} - V_{g1}^0)}{2k_B T}\right)}, \quad (\text{Q1})$$

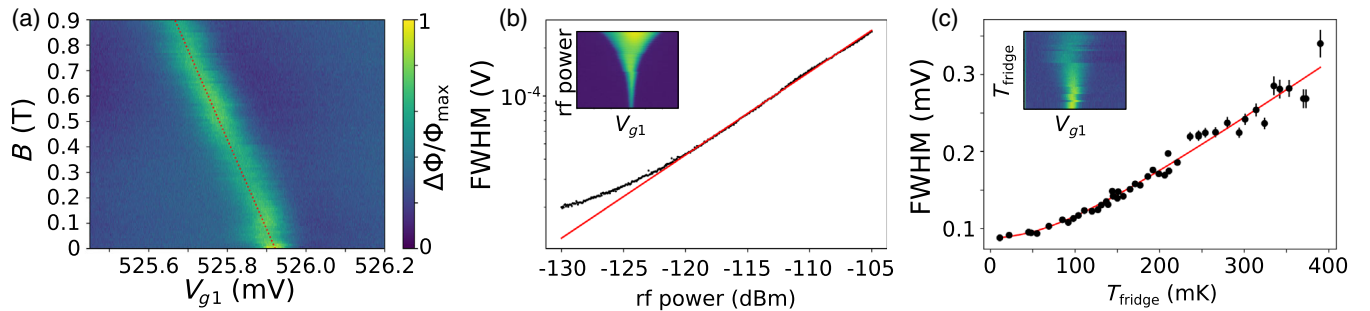


FIG. 17. SEB lever arm and electron temperature. (a) Magnetospectroscopy of dot-to-reservoir transition used to extract the SEB lever arm. (b) FWHM of the SEB transition as a function of rf power (raw data in inset). Above -120 dBm the deviation of the data (black dots) from the linear fit (red line) indicates the peak is power broadened; thus the temperature dependence of the FWHM in (c) was taken at -130 dBm. From the fit shown in red, we estimate a T_e of 115 ± 6 mK.

where V_{g1}^0 is the gate voltage at the center of the peak. The change in V_{g1}^0 due to the applied magnetic field B is directly related to the SEB's lever arm, as

$$g\mu_B\Delta B = e\alpha\Delta V_{g1}^0, \quad (\text{Q2})$$

where we take the electron g factor as 2, μ_B is the Bohr magneton, and e is the charge of an electron. From the fit, we extract an α of 0.40. To characterize the electron temperature T_e of the SEB, we measure the FWHM of the SEB as a function of mixing chamber fridge temperature T_{fridge} . To ensure the transition is not power broadened, we first measure the transition at varying rf powers at base temperature, as shown in Fig. 17(b). We determine that above -125 dBm the signal becomes power broadened, and thus we take temperature dependence measurements at -130 dBm. To extract the electron temperature T_e of the SEB, we fit the expression

$$\text{FWHM} = \frac{3.53k_B}{e\alpha} \sqrt{T_{\text{fridge}}^2 + T_e^2}, \quad (\text{Q3})$$

where k_B is the Boltzmann constant and e is the charge of an electron. From the fit in Fig. 17(c), we estimate an electron temperature of 115 ± 6 mK. Since we are thermally broadened, we estimate an upper bound for the tunneling rate $\gamma \leq 4.25$ GHz as

$$3.53k_B T_e \geq 2h\gamma. \quad (\text{Q4})$$

APPENDIX R: RESONATOR PARAMETER EXTRACTION USING KINETIC INDUCTANCE CHANGES

Because of the presence of uncalibrated standing waves in the reflected rf signal arising from impedance mismatch in the reflectometry setup, magnetospectroscopy of the reflected signal was taken up to 0.9 T, as shown in

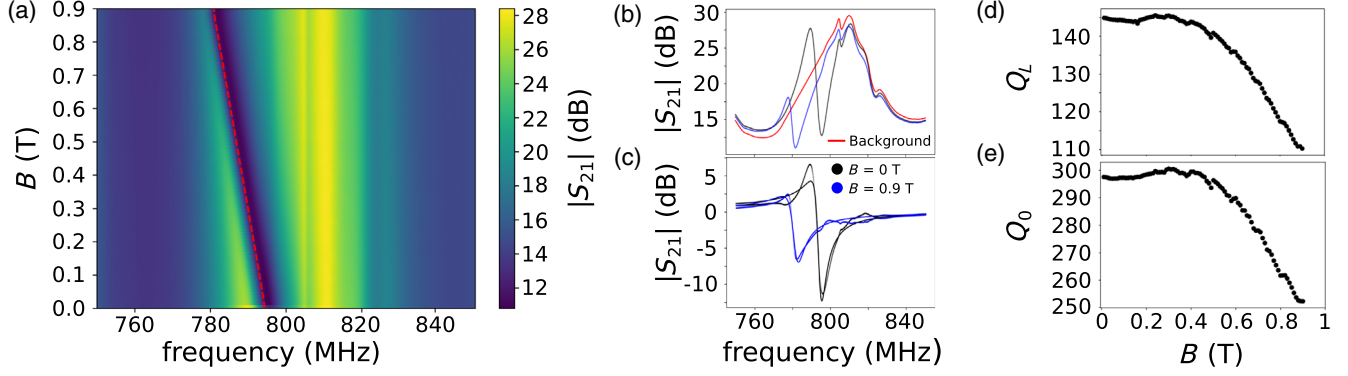


FIG. 18. Resonator parameter extraction. (a) Magneto spectroscopy of $|S_{21}|$ as a function of magnetic field B , resulting in a change in resonance frequency, as highlighted by the red dashed line. (b) $|S_{21}|$ at B fields of 0 T (black) and 0.9 T (blue) with the estimated background signal in red. (c) Background subtracted response with corresponding fits, from which the loaded Q_L (d) and internal Q_0 (e) quality factors are then extracted as a function of applied field B .

Fig. 18(a). We assume that the background remains constant while the resonance frequency shifts as a function of B field, allowing us to infer the background amplitude transfer function, as shown in Fig. 18(b). To account for any asymmetry in the line, we fit a complex external quality factor \tilde{Q}_e resulting in the fits shown in Fig. 18(c):

$$S_{21} = A \left(1 - \frac{2Q_L e^{i\phi}}{|\tilde{Q}_e| (1 + 2iQ_L \frac{f-f_r}{f_r})} \right). \quad (\text{R1})$$

The extracted parameters at zero field are a resonance frequency $f_r = 797$ MHz, a loaded quality factor Q_L of 145, and an external quality factor Q_e of 282, resulting in an intrinsic quality factor Q_0 of 298. We get a phase delay ϕ of 0.98 and an amplitude A of 17.2 dB, resulting in a matching β of 1.05. From the extracted values, we observe that there is no change in Q_L and Q_0 up to 0.4 T [Figs. 18(d) and 18(e)], above which the resonance appears to deteriorate, potentially due to vortex formation in the superconducting NbN inductor.

APPENDIX S: PID CONTROLLER

A proportional integral derivative controller is a closed-loop control system employing feedback to maintain a certain setpoint. In this particular implementation, we bias the SEB at the point of its maximum derivative of the magnitude of the reflective signal ΔA [red dot in Fig. 19(a)], as this is the most sensitive point. To increase the dynamic range of the PID controller, a large rf power of -100 dBm is applied to broaden the peak, resulting in a FWHM of 2 mV. Varying V_{g2} (and to a lesser extent V_{g3}) results in a large change in signal ΔA , as shown in Fig. 19(b), as it shifts the SEB bias point due to the QDs' cross capacitances. Based on the change in signal, the feedback loop compensates V_{g1} , as shown in Fig. 19(c), according to

$$V_{g1}(n+1) = V_{g1}(n) + m_i \Delta V_{gi} + P(n) + I(n) + D(n). \quad (\text{S1})$$

To ensure that the PID feedback loop does not go out of range, the controller output is bounded between minimum V_{g1}^{\min} and maximum V_{g1}^{\max} safety voltages, which are user defined. In Eq. (S1), $V_{g1}(n)$ is the voltage on the SEB at step n , m_i is the gradient due to the gate capacitance ratio between the SEB and QD_i , as estimated in Appendix U, and ΔV_{gi} is the gate voltage step taken on gate i , in this implementation $i = 2$ or 3 . Then, $P(n)$, $I(n)$, and $D(n)$ are the proportional, integral, and differential compensations at step n , which are defined as

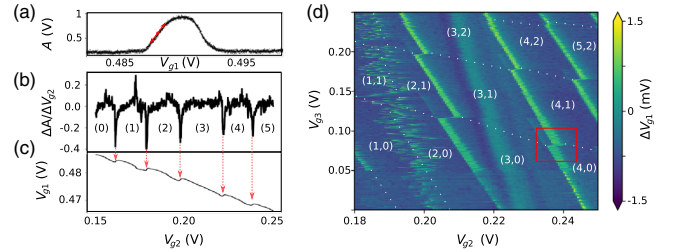


FIG. 19. PID charge sensing in the few-electron regime. (a) Normalized magnitude of the reflected signal of dot-to-reservoir transition line of the SEB used for charge sensing. The red dot shows the setpoint used for PID control, with arrows indicating how the signal varies as the peak shifts. (b) Change in magnitude response due to a change in V_{g2} with the electron occupancy in QD_2 in brackets. (c) PID response on V_{g1} due to the change in signal in (b), highlighted by the red arrows. (d) Differential of V_{g1} PID response due to a change in V_{g2} and V_{g3} , resulting in the stability diagram in the few-electron regime. We indicate the electron occupancy as well as a red rectangle highlighting the interdot charge transition used for single-shot readout.

$$\begin{aligned}
P(n) &= K_P \Delta A, \\
I(n) &= K_I \frac{\Delta V_{gi}}{2} [\Delta A(n) + \Delta A(n-1)] + I(n-1), \\
D(n) &= \frac{2K_D}{2\tau + \Delta V_{gi}} [\Delta A(n) - \Delta A(n-1)] \\
&\quad + \frac{2\tau - \Delta V_{gi}}{2\tau + \Delta V_{gi}} D(n-1), \tag{S2}
\end{aligned}$$

where K_P , K_I , and K_D are the proportional, integral, and differential coefficients, which have to be tuned by the user. Here, τ is the cutoff frequency of a low-pass filter used to reduce high frequency noise on the differential term. We use $\tau = 1$. The integrator part is limited via a dynamic integrator clamping scheme to ensure that no integration occurs if the signal is already saturated by $P(n)$,

$$I_{\max} = \max[V_{g1}^{\max} - V_{g1}(n+1) + I(n), 0], \tag{S3}$$

$$I_{\min} = \min[V_{g1}^{\min} - V_{g1}(n+1) + I(n), 0]. \tag{S4}$$

Once the PID is tuned, we acquire the charge stability diagram shown in Fig. 19(d). The PID performs well apart from the region corresponding to $1 \leftrightarrow 2$ charge transition of QD₂. Nevertheless, we accurately determine the location in gate voltage space of the (3,1)–(4,0) charge transition, as highlighted by the red box, as well as an estimate of the (1,1)–(2,0) transition.

APPENDIX T: VALLEY-ORBIT SPLITTING

From the estimated voltage space regions from the stability diagram using the PID controller in Fig. 19(d), we were able to locate the (1,1)–(2,0) and the (3,1)–(4,0) charge transitions, which exhibit PSB as shown in Figs. 20(a) and 20(b). By taking a vertical trace in the region of PSB, two Fermi-distribution-like functions are observed, as shown in Figs. 20(c) and 20(d). To extract the measurement window ΔV and the lever arm α of QD₃, the following function was fitted to the data:

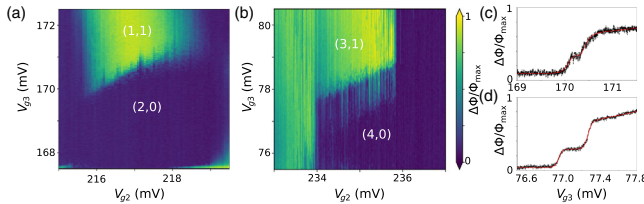


FIG. 20. Valley-orbit splitting of the (1,1)–(2,0) and (3,1)–(4,0) charge transitions. ICTs of (1,1)–(2,0) (a) and (3,1)–(4,0) (b) in which PSB is observed. Single traces taken while ramping V_{g3} along SPB for the (1,1)–(2,0) (c) and (3,1)–(4,0) (d). The double Fermi distribution function is then fitted to estimate the valley-orbit splittings as 15.6 and 195.5 μeV , respectively.

$$\Delta\Phi/\Phi_{\max} = m_1 F_1(V_{g3}) + c_1 + (m_2 V_{g3} + c_2) F_2(V_{g3}), \tag{T1}$$

where m_1 , m_2 , c_1 , and c_2 are fitting parameters for the linear gradients due to shifts in the charge sensor as a result of ramping V_{g3} . $F_i(V_{g3})$ is a Fermi distribution function centered at V_i^0 :

$$F_i(V_{g3}) = \frac{1}{\exp\left(\frac{e\alpha(V_{g3}-V_i^0)}{k_B T_e}\right) + 1}, \tag{T2}$$

where e is the charge of an electron, k_B is the Boltzmann constant, and T_e is the electron temperature, as determined in Appendix Q. From the fits in Figs. 20(c) and 20(d), we estimate a $\Delta V = (V_2^0 - V_1^0)$ of 113 and 374 μV and an α of 0.139 and 0.525, respectively. The valley-orbit splitting can then be evaluated as $e\alpha\Delta V$, giving an estimate of 15.6 and 195.5 μeV , respectively.

APPENDIX U: STRONG CHARGE SENSOR RESPONSE

By operating the QD₁ as a SEB, multiple dot-to-reservoir transitions can be used for charge sensing, as shown in Fig. 21(a). Typically, sensing is done with the most intense transition due to the higher signal-to-noise ratio. However, in our particular system, there is a positively sloped transition line that couples to the SEB, probably due to a defect in the silicon oxide. This line interacts with the SEB close to the $3 \leftrightarrow 4$ charge transition of QD₂ for the two most intense SEB lines in Fig. 21(a). As a result, we operate the SEB at the third most intense line, as highlighted by the red box. From this dataset, and a similar one of V_{g1} versus V_{g3} (not shown here), the gradients $\Delta V_{g1}/\Delta V_{g2}$ and $\Delta V_{g1}/\Delta V_{g3}$ were estimated as -0.237 and -0.034 , respectively. This was carried out by taking the Hough transform of the threshold dataset, as described in Ref. [61]. These slopes indicate QD₂ is 7 times more coupled to the SEB than QD₃. These slopes were later built in the charge sensing controller of Appendix S.

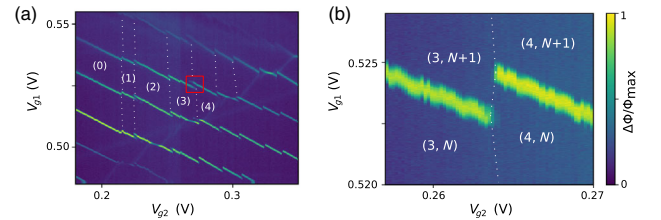


FIG. 21. Charge stability diagram QD₁ versus QD₂. (a) Highlighted charge sensing region of interest (red square) in the V_{g1} versus V_{g2} gate space. The numbers indicate the electron occupation in QD₂. (b) Enlarged measurement, highlighting the large charge response of the SEB when an electron is loaded onto QD₂. The numbers in parentheses indicate the electron occupation of QD₂ and QD₁, respectively.

From Fig. 21(b), we estimate the voltage shift in QD₁ when an electron is loaded into QD₂. This was done by fitting a \cosh^{-2} distribution to the SEB transition for varying V_{g2} voltages [Eq. (Q1)]. From the fits, we extract the center and FWHM of the transition line, resulting in a voltage shift ΔV_{g1} of 1.70 mV, which is almost 3 times the average FWHM of 0.64 mV. We also note that the FWHM is constant as a function of V_{g2} , indicating that the peak is thermally rather than lifetime broadened [44].

APPENDIX V: SINGLET-TRIPLET MODEL FOR PAULI SPIN BLOCKADE

For Pauli spin blockade, an analytical model to describe the probability density functions (PDFs) for both a singlet n_S and a triple n_T exists [35]. In the case of Gaussian noise

of equal strength in both quadratures (e.g., cryogenic amplifier noise limited), the singlet probability in the IQ plane reads

$$n_S(I, Q) = \frac{(1 - P_T)}{2\pi\sigma^2} \exp\left(-\frac{(I - I^S)^2}{2\sigma^2} - \frac{(Q - Q^S)^2}{2\sigma^2}\right), \quad (\text{V1})$$

where P_T is the probability of a triplet outcome, (I^S, Q^S) is the center of the singlet Gaussian in the IQ plane, and σ is the standard deviation of the distribution. For the triplet PDF, there is the added possibility of relaxation to a singlet during the measurement time Δt , resulting in two extra integral terms:

$$n_T(I, Q) = \frac{P_T}{2\pi\sigma^2} \exp\left(-\frac{\Delta t}{T_1}\right) \exp\left(-\frac{(I - I^T)^2}{2\sigma^2} - \frac{(Q - Q^T)^2}{2\sigma^2}\right) + \int_{I^S}^{I^T} \frac{\Delta t P_T}{T_1(I^T - I^S)} \exp\left(-\frac{I_x - I^S \Delta t}{I^T - I^S T_1}\right) \exp\left(-\frac{(I - I_x)^2}{2\sigma^2}\right) \frac{dI_x}{2\pi\sigma} \\ + \int_{Q^S}^{Q^T} \frac{\Delta t P_T}{T_1(Q^T - Q^S)} \exp\left(-\frac{Q_y - Q^S \Delta t}{Q^T - Q^S T_1}\right) \exp\left(-\frac{(Q - Q_y)^2}{2\sigma^2}\right) \frac{dQ_y}{2\pi\sigma}, \quad (\text{V2})$$

where the integral terms due to the triplet decaying into a singlet I_D (second and third addends) have an analytical solution:

$$I_D(V) = \frac{\Delta t P_T}{\sqrt{2\pi} T_1 (V^T - V^S)} \exp\left[\frac{\Delta t}{(V^T - V^S) T_1} \left(V^S - V + \frac{\Delta t \sigma^2}{2(V^T - V^S) T_1}\right)\right] \\ \times \left\{ \operatorname{erf}\left[\frac{\sigma \Delta t}{(V^T - V^S) T_1 \sqrt{2}} + \frac{V^T - V}{\sigma \sqrt{2}}\right] - \operatorname{erf}\left[\frac{\sigma \Delta t}{(V^T - V^S) T_1 \sqrt{2}} + \frac{V^S - V}{\sigma \sqrt{2}}\right] \right\}. \quad (\text{V3})$$

We use these equations to fit the outcome of the single shots in the IQ plane (the average signal over Δt). We extract the centers of the two distributions. We then project the data along the axis that connects both centers, to thus reduce the problem to one dimension, as in Barthel *et al.* [35] and, hence, reduce the number of fitting parameters to P_T , V^S , V^T , and σ . From the fitted parameters, we determine the singlet F_S and triplet F_T fidelities as a function of threshold voltage V_T above which we call the shot a triplet,

$$F_S = 1 - \int_{V_T}^{\infty} \frac{n_S(V)}{1 - P_T} dV = 1 - \frac{1}{2} \left[1 + \operatorname{erf}\left(\frac{V^S - V_T}{\sqrt{2}\sigma}\right) \right], \\ F_T = 1 - \int_{-\infty}^{V_T} \frac{n_T(V)}{P_T} dV \\ = 1 - \frac{1}{2} \exp\left(-\frac{\Delta t}{T_1}\right) \left[1 - \operatorname{erf}\left(\frac{V^T - V_T}{\sqrt{2}\sigma}\right) \right] \\ - \int_{-\infty}^{V_T} I_D(V) dV. \quad (\text{V4})$$

Here the integral for F_T has no analytical solution and thus needs to be computed numerically. The visibility V_E and the average spin measurement fidelity F_M are then determined as

$$V_E = \max[F_S(V_T) + F_T(V_T) - 1], \\ F_M = \max[(1 - P_T)F_S(V_T) + P_T F_T(V_T)]. \quad (\text{V5})$$

APPENDIX W: SIGNAL-TO-NOISE RATIO AND IDEAL FIDELITY

To extract the SNR for the SEB at various temperatures, each trace from the inset in Fig. 17(c) was plotted in the IQ plane, as shown in Fig. 22(a). Since we subtract the average background for the IQ data, the background noise forms a 2D Gaussian distribution centered at the origin. The circular shape shows the system is cryogenic amplifier noise limited. The standard deviation of the Gaussian distribution [dashed circle in Fig. 22(a)] represents the noise of the system, while the signal is measured as the

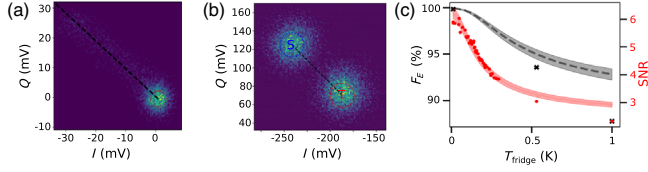


FIG. 22. SNR extraction for (a) dot-to-reservoir (DTR) transition on sensing QD and (b) single-shot data. (c) SNR data points as a function of temperature, with best fit (red line). From the fitted SNR data, the electrical fidelity was estimated for a measurement time Δt of $5.6 \mu\text{s}$ (black line). Black crosses are the measured electrical fidelity.

distance between the maximum value, obtained by fitting Eq. (Q1) to the I and Q data and the center of the noise, depicted by the black dashed line. A similar procedure is carried out for the single-shot data, after averaging the signal over the measurement time Δt , as shown in Fig. 22(b). The main difference is that two peaks appear, one due to the singlets and the other due to the triplets outcomes, which we fit according to Eqs. (V1) and (V2), respectively. The noise is still calculated as the fitted average standard deviation, while the signal is the distance between the two peaks. Since the two methods adopted to measure the SNR were carried out at two different rf powers and on different days, the SNR values extracted at base temperature were used to calibrate the two datasets, resulting in the red data points on Fig. 22(c). While the SEB peak shift remains greater than its FWHM, the SNR has the following temperature dependence:

$$\text{SNR} \propto \frac{1}{\sqrt{T_{\text{fridge}}^2 + T_e^2}}, \quad (\text{W1})$$

where the value extracted in Appendix Q was used for T_e , resulting in the fitted red curve. At 1 K the fitted SNR is larger than the measured one, suggesting that other factors may be deteriorating the overall SNR. From the SNR, one can then calculate the electrical fidelity F_E (assuming an infinite T_1), resulting in the blue dotted line:

$$F_E = \frac{1}{2} \left[1 + \text{erf} \left(\frac{\text{SNR}}{2\sqrt{2}} \right) \right]. \quad (\text{W2})$$

APPENDIX X: POSSIBLE ARCHITECTURES USING SEBs AS READOUT SENSORS

In this appendix, we analyze the benefits in scalability of using SEBs as readout sensors. We first focus on silicon nanowire devices (or nanowire devices in general) like the ones presented here. In these nanowires with a serial gate arrangement, like the one in Fig. 3(a), two SEBs can be implemented at the ends of the nanowire. On the contrary, SETs cannot be implemented.

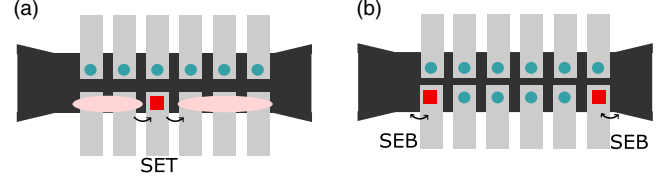


FIG. 23. Quantum-dot-based architectures in a nanowire. (a) The reservoirs are extended to form a SET on one side of the $2 \times N$ array [see Fig. 23(a)]. However, that neutralizes the use of one side of the array as quantum dots. By comparison, two (or four) SEBs can be formed at the edges of the nanowire enabling the use of the central quantum dots for computation [see Fig. 23(b)].

On the other hand, the devices with split-gate geometry, like the one in Fig. 23, enable forming one SET on one side of the $2 \times N$ array [see Fig. 23(a)]. However, that neutralizes the use of one side of the array as quantum dots. By comparison, two (or four) SEBs can be formed at the edges of the nanowire enabling the use of the central quantum dots for computation [see Fig. 23(b)].

For more generic linear geometries, we compare the role of different sensors considering planar silicon. Figure 24 focuses on a linear array of QDs similar to the approach presented in Refs. [62,63]. The upper part of the structure has plunger gates alternated with barrier gates to define few-electron QDs (blue circles) and its lower part includes the charge sensors (red squares). Figure 24(a) shows an example of this implementation with SETs, leading to one sensor for every three qubits. On the other hand, Fig. 24(b) shows how the structure would look when using SEBs. The sensor-to-qubit ratio increases when using SEBs, having one sensor every two qubits.

We now explore new architectures that can be produced in planar geometries with plug-on gates (available in the 10 nm node and below). SEBs only need one reservoir for readout, which can unlock structures like the one shown in Fig. 25(a), where a single reservoir is shared between four SEBs. This structure is the center part of the design, where a reservoir, sketched as a light red rectangle, is surrounded by four SEBs (red squares). We consider each SEB can act primarily as a charge sensor for its three nearest neighbor qubits, represented as dark blue circles in Fig. 25(b). Qubit

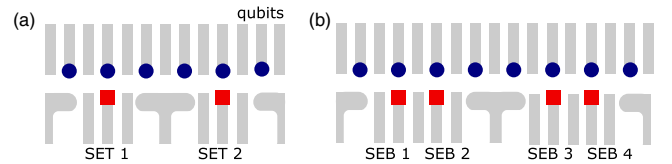


FIG. 24. Readout architectures in a linear array of QDs. (a) Qubits, pictured as blue circles, sensed by SETs (red squares). The SETs are placed between accumulated reservoirs (T-shaped gates) and have barrier gates to control the tunnel rate. (b) A similar structure with SEBs. The structure presents a gate between every pair of SEBs for isolation.

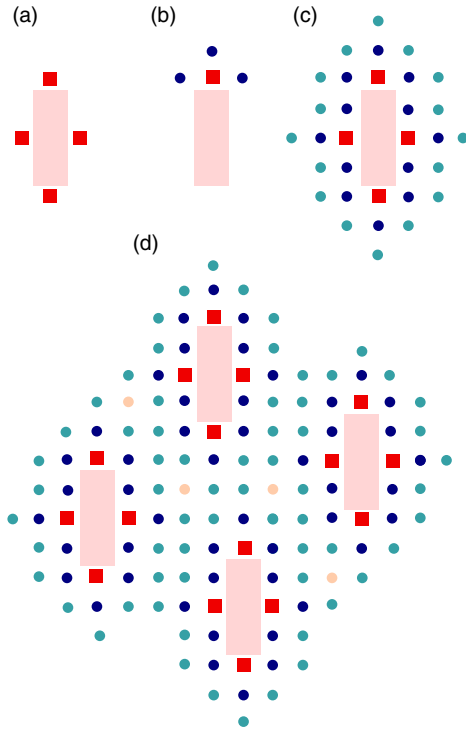


FIG. 25. Two-dimensional architecture with SEBs. (a) Reservoir, pictured as a light red rectangle, shared between four SEBs (red squares). (b) SEB, reservoir, and qubit dots that can be directly charge sensed by the SEB (dark blue circles). (c) Unit cell: sensing structure surrounded by ancilla qubits for PSB readout (dark blue) and data qubits (light blue). (d) A 4 unit cell architecture. As observed in the picture, most qubit dots can be read via PSB. The qubits that do not belong to a PSB couple are pictured as yellow circles (1 per unit cell).

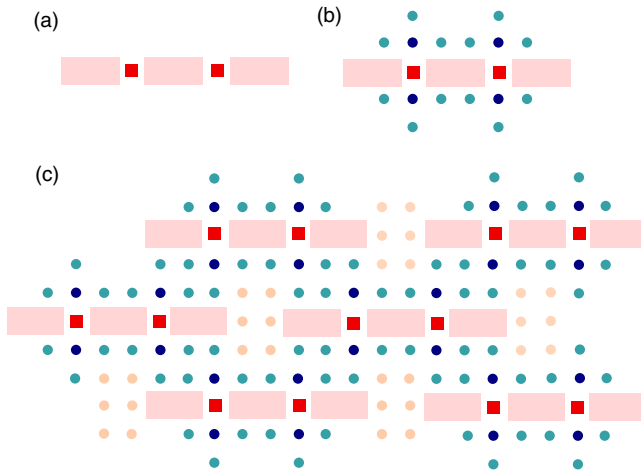


FIG. 26. Two-dimensional architecture with SETs. (a) SETs (red squares) placed in between reservoirs (light red rectangles). (b) Unit cell: sensing structure surrounded by qubit dots. The dark blue circles correspond to the qubits that can be directly charge sensed. The light blue circles are the qubits that can be readout through PSB. (c) A 6 unit cell architecture. The yellow circles correspond to the qubits that cannot be readout via PSB projection.

readout could be based on Pauli spin blockade between couples of nearest neighbor qubits, where the light blue circles represent data qubits and the dark blue circles the ancilla qubits for PSB projection. Figure 25(c) shows the sensing structure with all the qubits that can be read via PSB. Although the 4 SEBs plus reservoir occupy a small area (7 grid squares), they still can charge sense 12 qubits (dark blue circles) that can be used to project a total of 16 data qubits. Building on a grid formed by these structures, we envision an architecture with high qubit connectivity in which most qubits are part of a PSB couple apart from a small subset (1 per unit cell) indicated in yellow.

Figure 26 introduces a similar architecture using SETs as charge sensors. Figure 26(b) shows that the additional reservoirs that SETs require deteriorate the ratio between the sensing structure area (8 grid squares [64]), the number of charge-detectable qubits (4 qubits), and the number of qubit dots that can be read via PSB (12 qubits). This compromises the ability to have simultaneously high qubit connectivity and readability. Figure 26(c) shows that to achieve similar connectivity, not all the qubits can be directly read out via PSB (yellow circles), in this case, 6 per unit cell.

- [1] X. Xue, M. Russ, N. Samkharadze, B. Undseth, A. Sammak, G. Scappucci, and L. M. K. Vandersypen, *Quantum Logic with Spin Qubits Crossing the Surface Code Threshold*, *Nature (London)* **601**, 343 (2022).
- [2] A. Noiri, K. Takeda, T. Nakajima, T. Kobayashi, A. Sammak, G. Scappucci, and S. Tarucha, *Fast Universal Quantum Gate Above the Fault-Tolerance Threshold in Silicon*, *Nature (London)* **601**, 338 (2022).
- [3] A. R. Mills *et al.*, *Two-Qubit Silicon Quantum Processor with Operation Fidelity Exceeding 99%*, *Sci. Adv.* **8**, 14 (2022).
- [4] M. Veldhorst, H. G. J. Eenink, C. H. Yang, and A. S. Dzurak, *Silicon CMOS Architecture for a Spin-Based Quantum Computer*, *Nat. Commun.* **8**, 1766 (2017).
- [5] J. M. Boter *et al.*, *Spiderweb Array: A Sparse Spin-Qubit Array*, *Phys. Rev. Appl.* **18**, 024053 (2022).
- [6] R. Maurand *et al.*, *A CMOS Silicon Spin Qubit*, *Nat. Commun.* **7**, 13575 (2016).
- [7] A. M. J. Zwerver *et al.*, *Qubits Made by Advanced Semiconductor Manufacturing*, *National electronics review* **5**, 184 (2022).
- [8] A. Ruffino *et al.*, *A cryo-CMOS Chip That Integrates Silicon Quantum Dots and Multiplexed Dispersive Readout Electronics*, *National electronics review* **5**, 53 (2022).
- [9] S. McArdle, X. Yuan, and S. Benjamin, *Error-Mitigated Digital Quantum Simulation*, *Phys. Rev. Lett.* **122**, 180501 (2019).
- [10] L. Botelho, A. Glos, A. Kundu, J. A. Miszczak, O. Salehi, and Z. Zimborás, *Error Mitigation for Variational Quantum Algorithms through Mid-Circuit Measurements*, *Phys. Rev. A* **105**, 022441 (2022).

- [11] Y. Wan *et al.*, *Quantum Gate Teleportation between Separated Qubits in a Trapped-Ion Processor*, *Science* **364**, 875 (2019).
- [12] M. J. Curry *et al.*, *Single-Shot Readout Performance of Two Heterojunction-Bipolar-Transistor Amplification Circuits at Millikelvin Temperatures*, *Sci. Rep.* **9**, 16976 (2019).
- [13] E. J. Connors, J. Nelson, and J. M. Nichol, *Rapid High-Fidelity Spin-State Readout in Si/Si-Ge Quantum Dots via rf Reflectometry*, *Phys. Rev. Appl.* **13**, 024019 (2020).
- [14] K. D. Petersson, C. G. Smith, D. Anderson, P. Atkinson, G. A. C. Jones, and D. A. Ritchie, *Charge and Spin State Readout of a Double Quantum Dot Coupled to a Resonator*, *Nano Lett.* **10**, 2789 (2010).
- [15] J. I. Colless, A. C. Mahoney, J. M. Hornibrook, A. C. Doherty, H. Lu, A. C. Gossard, and D. J. Reilly, *Dispersive Readout of a Few-Electron Double Quantum Dot with Fast rf Gate Sensors*, *Phys. Rev. Lett.* **110**, 046805 (2013).
- [16] M. F. Gonzalez-Zalba, S. Barraud, A. J. Ferguson, and A. C. Betz, *Probing the Limits of Gate-Based Charge Sensing*, *Nat. Commun.* **6**, 6084 (2015).
- [17] M. G. House, I. Bartlett, P. Pakkiam, M. Koch, E. Peretz, J. van der Heijden, T. Kobayashi, S. Rogge, and M. Y. Simmons, *High-Sensitivity Charge Detection with a Single-Lead Quantum Dot for Scalable Quantum Computation*, *Phys. Rev. Appl.* **6**, 044016 (2016).
- [18] M. Urdampilleta *et al.*, *Gate-Based High Fidelity Spin Readout in a CMOS Device*, *Nat. Nanotechnol.* **14**, 737 (2019).
- [19] E. Chanrion, D. J. Niegemann, B. Bertrand, C. Spence, B. Jadot, J. Li, P. A. Mortemousque, L. Hutin, R. Maurand, X. Jehl *et al.*, *Charge Detection in an Array of CMOS Quantum Dots*, *Phys. Rev. Appl.* **14**, 024066 (2020).
- [20] F. Ansaloni, A. Chatterjee, H. Bohuslavskiy, B. Bertrand, L. Hutin, M. Vinet, and F. Kuemmeth, *Single-Electron Operations in a Foundry-Fabricated Array of Quantum Dots*, *Nat. Commun.* **11**, 6399 (2020).
- [21] V. N. Ciriano-Tejel *et al.*, *Spin Readout of a CMOS Quantum Dot by Gate Reflectometry and Spin-Dependent Tunnelling*, *PRX Quantum* **2**, 010353 (2021).
- [22] F. Borjans, X. Mi, and J. Petta, *Spin Digitizer for High-Fidelity Readout of a Cavity-Coupled Silicon Triple Quantum Dot*, *Phys. Rev. Appl.* **15**, 044052 (2021).
- [23] G. Zheng, N. Samkharadze, M. L. Noordam, N. Kalhor, D. Brousse, A. Sammak, G. Scappucci, and L. M. K. Vandersypen, *Rapid Gate-Based Spin Read-Out in Silicon Using an On-Chip Resonator*, *Nat. Nanotechnol.* **14**, 742 (2019).
- [24] R. Vijay, M. H. Devoret, and I. Siddiqi, *Invited Review Article: The Josephson Bifurcation Amplifier*, *Rev. Sci. Instrum.* **80**, 111101 (2009).
- [25] F. Vigneau *et al.*, *Probing Quantum Devices with Radio-Frequency Reflectometry*, [arXiv:2202.10516](https://arxiv.org/abs/2202.10516).
- [26] D. Keith, M. G. House, M. B. Donnelly, T. F. Watson, B. Weber, and M. Y. Simmons, *Single-Shot Spin Readout in Semiconductors Near the Shot-Noise Sensitivity Limit*, *Phys. Rev. X* **9**, 041003 (2019).
- [27] S. Schaal, I. Ahmed, J. A. Haigh, L. Hutin, B. Bertrand, S. Barraud, M. Vinet, C. M. Lee, N. Stelmashenko, J. W. A. Robinson *et al.*, *Fast Gate-Based Readout of Silicon Quantum Dots Using Josephson Parametric Amplification*, *Phys. Rev. Lett.* **124**, 067701 (2020).
- [28] J. Stehlik, Y.-Y. Liu, C. M. Quintana, C. Eichler, T. R. Hartke, and J. R. Petta, *Fast Charge Sensing of a Cavity-Coupled Double Quantum Dot Using a Josephson Parametric Amplifier*, *Phys. Rev. Appl.* **4**, 014018 (2015).
- [29] J. M. Elzerman, R. Hanson, L. H. Willems van Beveren, B. Witkamp, L. M. K. Vandersypen, and L. P. Kouwenhoven, *Single-Shot Read-Out of an Individual Electron Spin in a Quantum Dot*, *Nature (London)* **430** (2004).
- [30] C. Barthel, M. Kjaergaard, J. Medford, M. Stopa, C. M. Marcus, M. P. Hanson, and A. C. Gossard, *Fast Sensing of Double-Dot Charge Arrangement and Spin State with a Radio-Frequency Sensor Quantum Dot*, *Phys. Rev. B* **81**, 161308(R) (2010).
- [31] T. Struck, J. Lindner, A. Hollmann, F. Schauer, A. Schmidbauer, D. Bougeard, and L. R. Schreiber, *Robust and Fast Post-Processing of Single-Shot Spin Qubit Detection Events with a Neural Network*, *Sci. Rep.* **11**, 16203 (2021).
- [32] Y. Matsumoto, T. Fujita, A. Ludwig, A. D. Wieck, K. Komatani, and A. Oiwa, *Noise-Robust Classification of Single-Shot Electron Spin Readouts Using a Deep Neural Network*, *npj Quantum Inf.* **7**, 136 (2021).
- [33] C. Yang, W. Lim, F. Zwanenburg, and A. Dzurak, *Dynamically Controlled Charge Sensing of a Few-Electron Silicon Quantum Dot*, *AIP Adv.* **1**, 042111 (2011).
- [34] A. West *et al.*, *Gate-Based Single-Shot Readout of Spins in Silicon*, *Nat. Nanotechnol.* **14**, 437 (2019).
- [35] C. Barthel, D. Reilly, C. M. Marcus, M. Hanson, and A. Gossard, *Rapid Single-Shot Measurement of a Singlet-Triplet Qubit*, *Phys. Rev. Lett.* **103**, 160503 (2009).
- [36] C. H. Yang *et al.*, *Operation of a Silicon Quantum Processor Unit Cell Above One Kelvin*, *Nature (London)* **580**, 350 (2020).
- [37] L. Petit, H. G. J. Eenink, M. Russ, W. I. L. Lawrie, N. W. Hendrickx, S. G. J. Philips, J. S. Clarke, L. M. K. Vandersypen, and M. Veldhorst, *Universal Quantum Logic in Hot Silicon Qubits*, *Nature (London)* **580**, 355 (2020).
- [38] M. F. Gonzalez-Zalba, S. de Franceschi, E. Charbon, T. Meunier, M. Vinet, and A. S. Dzurak, *Scaling Silicon-Based Quantum Computing Using CMOS Technology*, *National electronics review* **4**, 872 (2021).
- [39] X. Xue *et al.*, *CMOS-Based Cryogenic Control of Silicon Quantum Circuits*, *Nature (London)* **593**, 205 (2021).
- [40] M. Veldhorst *et al.*, *A Two-Qubit Logic Gate in Silicon*, *Nature (London)* **526**, 410 (2015).
- [41] P. G. J. Stephan *et al.*, *Universal Control of a Six-Qubit Quantum Processor in Silicon*, *Nature (London)* **609**, 919 (2022).
- [42] I. Ahmed *et al.*, *Radio-Frequency Capacitive Gate-Based Sensing*, *Phys. Rev. Appl.* **10**, 014018 (2018).
- [43] D. J. Ibberson *et al.*, *Large Dispersive Interaction between a CMOS Double Quantum Dot and Microwave Photons*, *PRX Quantum* **2**, 020315 (2021).
- [44] I. Ahmed, *Radio-Frequency Capacitive Gate-Based Sensing for Silicon CMOS Quantum Electronics*, Ph. D. Thesis, Cambridge University, 2018.
- [45] V. Derakhshan Maman, M. F. Gonzalez-Zalba, and A. Pályi, *Charge Noise and Overdrive Errors in Dispersive Readout*

- of Charge, Spin, and Majorana Qubits*, *Phys. Rev. Appl.* **14**, 064024 (2020).
- [46] S. N. Shevchenko, S. Ashhab, and F. Nori, *Landau-Zener-Stückelberg Interferometry*, *Phys. Rep.* **492**, 1 (2010).
- [47] S. Simbierowicz, V. Vesterinen, L. Grönberg, J. Lehtinen, M. Prunnila, and J. Hassel, *A Flux-Driven Josephson Parametric Amplifier for Sub-GHz Frequencies Fabricated with Side-Wall Passivated Spacer Junction Technology*, *Supercond. Sci. Technol.* **31**, 105001 (2018).
- [48] D. Pozar, *Microwave Engineering*, 4th ed. (John Wiley and Sons, New York, 2011).
- [49] P. J. Petersan and S. M. Anlage, *Measurement of Resonant Frequency and Quality Factor of Microwave Resonators: Comparison of Methods*, *J. Appl. Phys.* **84**, 3392 (1998).
- [50] S. Probst, F. B. Song, P. A. Bushev, A. V. Ustinov, and M. Weides, *Efficient and Robust Analysis of Complex Scattering Data under Noise in Microwave Resonators*, *Rev. Sci. Instrum.* **86**, 024706 (2015).
- [51] M. S. Khalil, M. J. A. Stoutimore, F. C. Wellstood, and K. D. Osborn, *An Analysis Method for Asymmetric Resonator Transmission Applied to Superconducting Devices*, *J. Appl. Phys.* **111**, 054510 (2012).
- [52] C. Deng, M. Otto, and A. Lupascu, *An Analysis Method for Transmission Measurements of Superconducting Resonators with Applications to Quantum-Regime Dielectric-Loss Measurements*, *J. Appl. Phys.* **114**, 054504 (2013).
- [53] S. Porbst, Resonator Tools, https://github.com/sebastianprobst/resonator_tools.
- [54] R. Hanson, L. P. Kouwenhoven, J. R. Petta, S. Tarucha, and L. M. K. Vandersypen, *Spins in Few-Electron Quantum Dots*, *Rev. Mod. Phys.* **79**, 1217 (2007).
- [55] L. Kranz, S. K. Gorman, B. Thorgrimsson, Y. He, D. Keith, J. G. Keizer, and M. Y. Simmons, *Exploiting a Single Crystal Environment to Minimize the Charge Noise on Qubits in Silicon*, *Adv. Mater.* **32**, e2003361 (2020).
- [56] S. W. Smith, *The Scientist and Engineer's Guide to Digital Signal Processing*, www.DSPguide.com.
- [57] P. Huang and X. Hu, *Electron Spin Relaxation due to Charge Noise*, *Phys. Rev. B* **89**, 195302 (2014).
- [58] H. Ismail Fawaz *et al.*, *inceptionTime: Finding AlexNet for Time Series Classification*, *Data Min. Knowl. Discov.* **34**, 1936 (2020).
- [59] I. Oguiza, *TSAT—A State-of-the-Art Deep Learning Library for Time Series and Sequential Data*, <https://github.com/timeseriesAI/tsai>.
- [60] L. Biewald, *Experiment Tracking with Weights and Biases*, <https://www.wandb.com/>.
- [61] G. A. Oakes *et al.*, *Automatic Virtual Voltage Extraction of a $2 \times N$ Array of Quantum Dots with Machine Learning*, [arXiv:2012.03685](https://arxiv.org/abs/2012.03685).
- [62] D. M. Zajac, T. M. Hazard, X. Mi, E. Nielsen, and J. R. Petta, *Scalable Gate Architecture for Densely Packed Semiconductor Spin Qubits*, *Phys. Rev. Appl.* **6**, 054013 (2016).
- [63] A. R. Mills, D. M. Zajac, M. J. Gullans, F. J. Schupp, T. M. Hazard, and J. R. Petta, *Shuttling a Single Charge across a One-Dimensional Array of Silicon Quantum Dots*, *Nat. Commun.* **10**, 1063 (2019).
- [64] Note that we intentionally reduced the size of the reservoirs to favor the SET architecture.